Tectonic Provenance of the Palaeoproterozoic Plum Tree Volcanics: Implications for the initiation of the McArthur Basin

Thesis submitted in accordance with the requirements of the University of Adelaide for an Honours Degree in Geology

Dion Higgie

November 2018

THE UNIVERSITY
of ADELAIDE

TECTONIC PROVENANCE OF THE PALAEOPROTEROZOIC PLUM TREE VOLCANICS: IMPLICTIONS FOR THE INITIATION OF THE MCARTHUR BASIN

RUNNING TITLE
Tectonic Provenance of the Plum Tree Volcanics

ABSTRACT
The Palaeoproterozoic (1825 ±4Ma) Plum Tree Volcanics are a bimodal suite of basalt and rhyolite lavas forming part of the fluvial conglomerate-sandstone sequence of the upper Edith River Group. They are preserved in remnants uncomformably overlying the Pine Creek Orogen north of Katherine in the Edith River, Mt Callanan and Birdie Creek basins. These sequences directly postdate the convergent orogenesis of the Pine Creek and mark the beginning of the extensional regime that initiated the McArthur Basin. The tectonic setting of the Plum Tree volcanism; whether divergent intraplate rift or mantle hotspot, may suggest how the formation of the McArthur Basin began and provide insight into how the Pine Creek Orogen compression ceased.

In this paper, geochemical methods were used to determine the tectonic setting of the Plum Tree Volcanics. Whole rock geochemical data was collected via XRF, ICP-MS and ICP-OES. Nd-Sm and Sr isotopic data was collected via column chromatography and TIMS. Petrographic data was collected via optical petrography.

Radiogenic Sr ($^{87}Sr/^{86}Sr$= ~0.708) and non-radiogenic Nd ($\varepsilon Nd_{(i)}$= -6 to -8) isotopes suggest a crustal component in melt evolution. Modelling of melt evolution by pure fractional crystallisation presents well-fitting liquid lines of descent, suggesting a fractional crystallisation driven melt evolution. Tholeiitic basalts and trace element geochemistry suggests a mantle derived melt driven by a mantle plume and intraplate continental rifting. Modelling of AFC processes suggest a lower crust sourced assimilant. Ambiguous basalt geochemistry supports a continental rift derived melt and an oxygen fugacity of FMQ -1 suggests a primitive, reduced melt reflecting a mantle parent. Optical petrography presents a plagioclase and clinopyroxene rich mineral assemblage reflecting a mantle parent.

KEYWORDS
Palaeoproterozoic, Geochemistry, Sr-Nd-Sm Isotopes, Bimodal Volcanism, McArthur Basin, Pine Creek Orogen, Plum Tree Volcanics, Rhyolite-MELTS, IgPet, Tectonic Provenance

CONTENTS

LIST OF FIGURES AND TABLES

INTRODUCTION

This project set out to determine the tectonic setting of the Plum Tree Volcanics at the base of the Proterozoic McArthur Basin using geochemical and radiogenic isotopic methods. The Plum Tree Volcanics (PTV) are a suite of bimodal volcanics ~30km north of Katherine, Northern Territory (Figure 1, Figure 2). Bimodal volcanism is the eruption of mafic and felsic lavas, with limited eruption of associated intermediate silica. This form of volcanism is known to be associated with various tectonic settings; including divergent intraplate rifts, convergent arc settings, and mantle hotspots. There have been few prior studies on the PTV, limited to Needham et al's (1985, 1988) studies on the tectonic evolution of the area, and a U-Pb SHRIMP age between 1822 ±5Ma and 1825 ±4Ma (Page, 1996a).
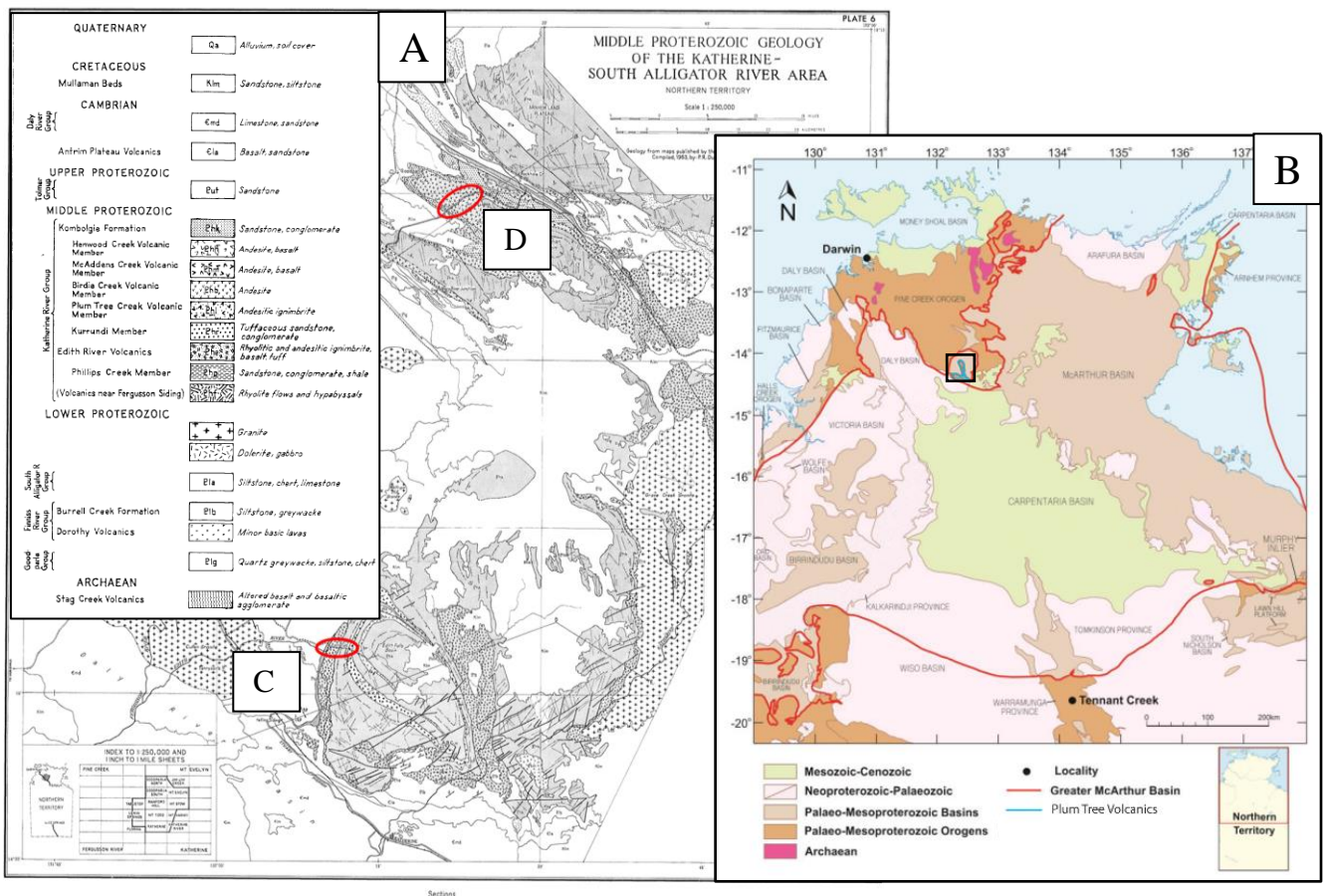
Figure 1: Map of the field localities in the Northern Territory. (A) Shows the region with the two field areas (magnified in Figure 2). (B) Shows the study location in the Northern Territory (highlighted with a black box) and the Plum Tree Volcanics (blue outline) and their location with respect to the Greater McArthur Basin (red outline). NT-wide map adapted from (Bullen, 2017).
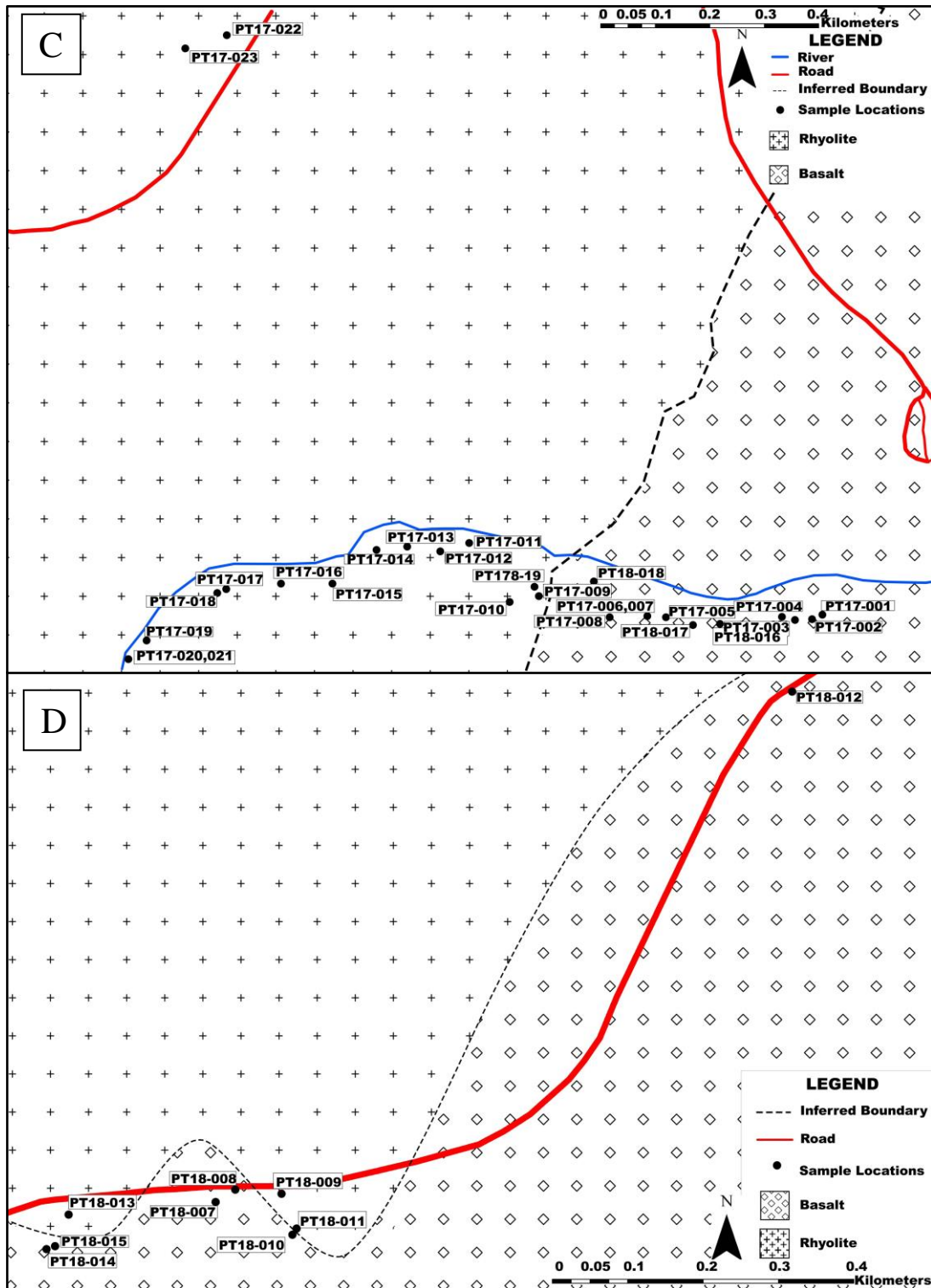
Figure 2: Magnified maps of the two main field localities. (C) Shows the Edith River at Edith Falls and the location of samples along this river. (D) shows the road corridor towards Kakadu National Park and the location of samples along the road. (Coordinates for field localities in Appendix A)

Rhyolites are often the result of fractional crystallisation of a mafic melt of mantle origin (Lacasse et al., 2006). Alternatively, progressive change of isotopic and trace element compositions coupled to indices of fractionation such as increasing SiO_2 or decreasing MgO often suggests a crustal component in rhyolite genesis. Fractional crystallisation is frequently accompanied by assimilation of continental crust (AFC) (DePaolo, 1981). Another model suggests that these hot mantle-derived melts cause anatexis in the felsic continental crust during ascent, thus generating felsic magmas (Pankhurst, 1995). In this model, there may be a sharp contrast in the isotopic and trace element composition of the mafic and felsic suite members.

These contrasting petrogenetic mechanisms can be distinguished by geochemical and isotopic data. Mantle derived melts have different isotopic ratios than those sourced from subducting oceanic slabs or from continental crust. REE patterns of melts sourced from hotspot or intraplate continental rift settings are 'seagull-like' (Figure 3), whereas convergent settings depict depleted MREE and HREE patterns (Bachmann & Bergantz, 2008).
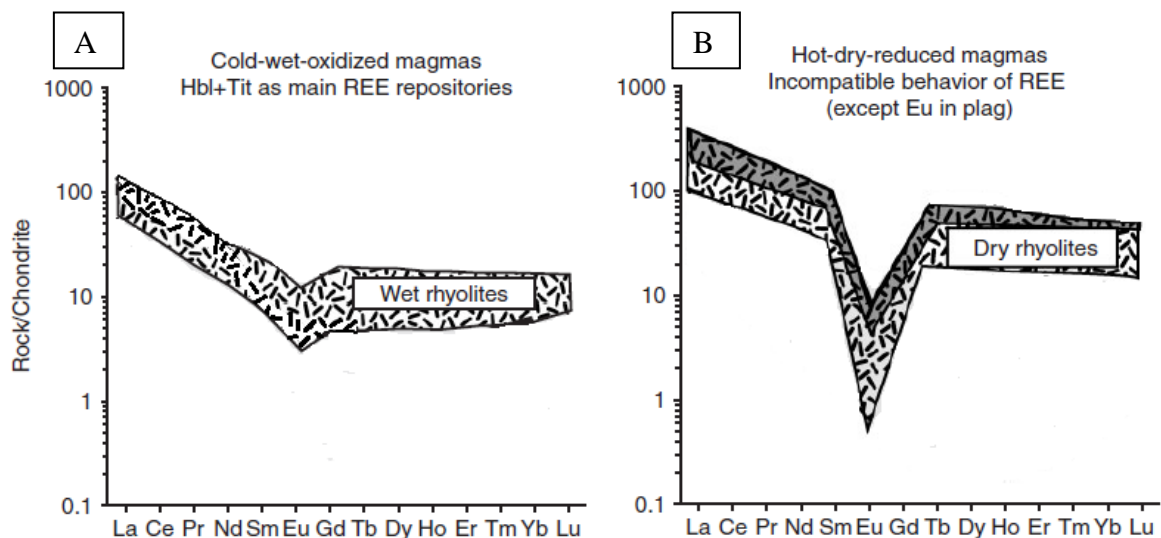
Figure 3: Typical REE patterns for rhyolites from different tectonic settings. (A) Shows rhyolite REE patterns typical of convergent settings. (B) Shows the 'seagull-like' REE patterns typical of hotspot and intraplate rift settings. Adapted from Bachmann & Bergantz (2008).

In this paper, geochemical methods were used to determine the origin of these volcanics. Geochemical and isotopic data was collected through standard geochemical methods and Nd-Sm and Sr isotopic analysis. Petrographic data was collected via thin section analysis. This data was used to determine whether the parent magma was either of rift, plume or subduction origin. The data was compared with Pine Creek Orogen basement to determine the role of crustal contamination on the genesis of this suite. The data was compared with analyses of similar aged volcanic suites in the McArthur Basin and other formations around Australia to determine their equivalence, and if there are correlatives in other basins and inliers. The data was also compared with contemporary bimodal volcanic suites to determine the tectonic provenance of these rocks.

GEOLOGICAL SETTING AND BACKGROUND

Edith River Group

The Edith River Group (ERG) is mostly made up of fluvial conglomerate, sandstone, siltstone, and shale units below the PTV. The Hindrance Creek Sandstone is a medium-coarse grained quartz sandstone that comprises the base of the ERG. The Kurrundie Sandstone above this is a thickly bedded purple-brown coarse-grained sandstone interbedded with conglomerate and siltstone. The Phillips Creek Sandstone is an interbedded sandstone, conglomerate and siltstone unit unconformably overlain by the PTV (M. Ahmad & Munson, 2013).

Unconformably underlying the ERG group is the El Sherana Group, which was deformed by the Maud Creek Event prior to the deposition of the ERG (Needham, Stuart-Smith, & Page, 1988). The folds associated with this event appear to be related to the emplacement of granites prior to the deposition of the Edith River Group in a series of fault bounded extensional basins that followed the Nimbuwah event (Needham & Stuart-Smith, 1985;

Worden et al., 2008). These basins were formed by rifting along the NW-SE and NNE-SSW

axes and reactivation of normal faults (Needham et al., 1988).

PLUM TREE VOLCANICS

The Plum Tree Volcanics are at the base of the McArthur Basin sequence. The PTV is

primarily made up of rhyolites and rhyolite ignimbrites, with basalts and basaltic andesites

also present. The volcanics are interbedded with terrestrial and fluvial sediments along the

northeast margin of the Mt Callanan Basin (Needham et al., 1988).

The suite's thickness ranges from 400 to 1000m and covers an estimated 6000 km^3 (Needham

& Stuart-Smith, 1985). It lies conformably on the sandstones that make up the lower Edith

River Group and uncomformably on the Cullen Batholith of the Pine Creek Orogen in the

north east (Needham & Stuart-Smith, 1985). The Katherine River Group of the McArthur

Basin disconformably overlies the Edith River Group to the north (Rawlings, 1999).

Pine Creek Orogen

The Pine Creek Orogen is a Neoarchean- Palaeoproterozoic (Hollis, Carson, & Glass, 2009)

orogen in the Northern Territory. The ERG has previously been classified as the top of the

Pine Creek Orogen stratigraphy (Figure 5) (Worden et al., 2008). The remaining formations

that make up the upper Pine Creek Orogen are largely intrusive granitoids and metasediments

(Worden et al., 2008). During the formation of the ERG was the intrusion of syn- and post-

tectonic granitoid plutons across the Pine Creek Orogen (Worden et al., 2008). The ERG is

located within the South Alligator Valley region of the Pine Creek Orogen's Central Domain.

The South Alligator Valley formed as a result of reactivation of normal faulting and the

formation of a wide, shallow NW-SE graben (Needham et al., 1988).
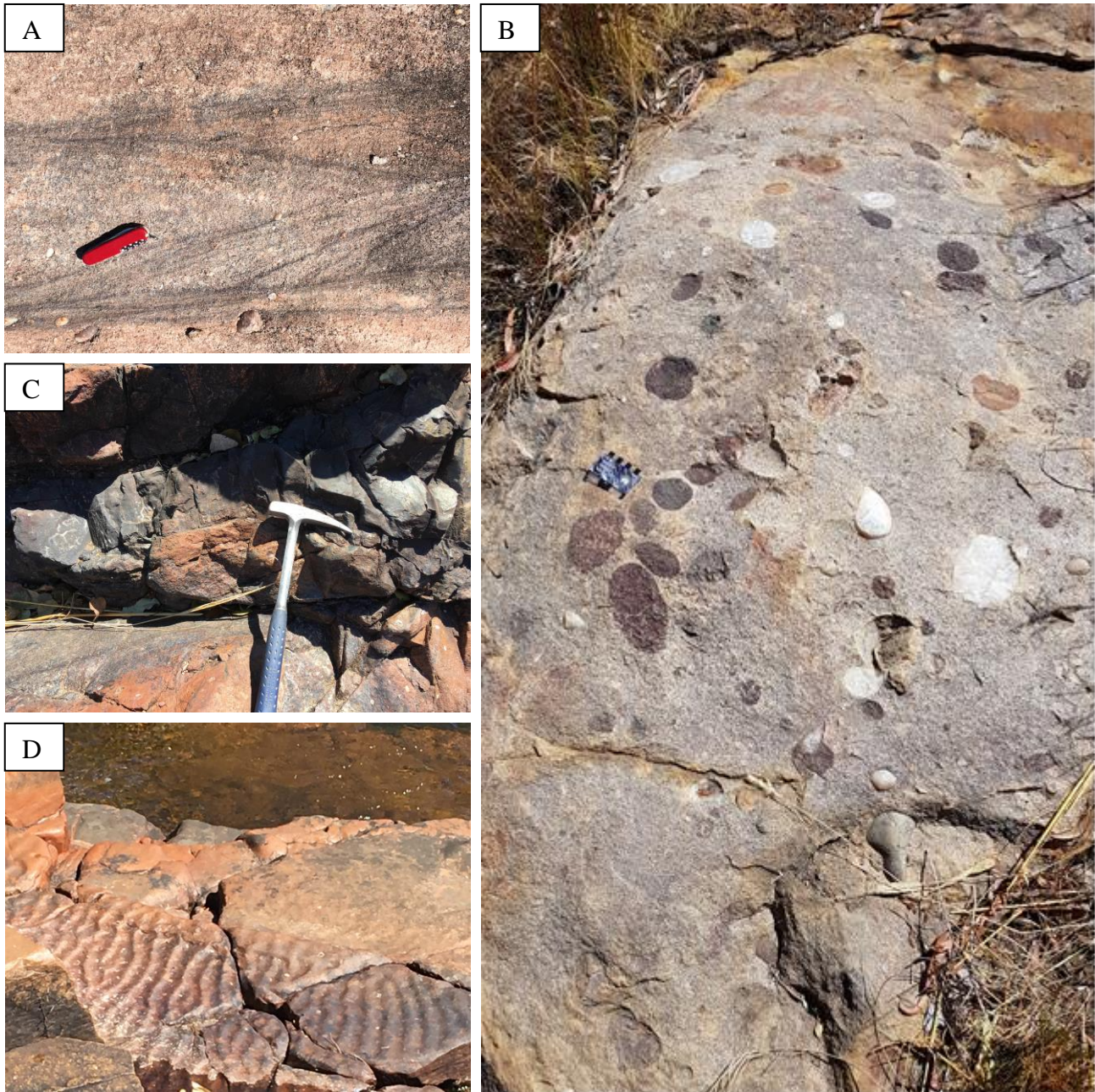
Figure 4: Field photographs of the PTV and overlying units. (A) Shows the trough cross-bedded basal sandstone of the Kombolgie Subgroup overlying the Edith River Group. (B) Shows the directly overlying fluvial conglomerate unit with clasts of volcanics embedded. (C) Shows a mafic dyke (middle) crosscutting the PTV rhyolite. (D) Shows rippled marked sandstone overlying the ERG suggesting a possible shallow marine depositional environment.
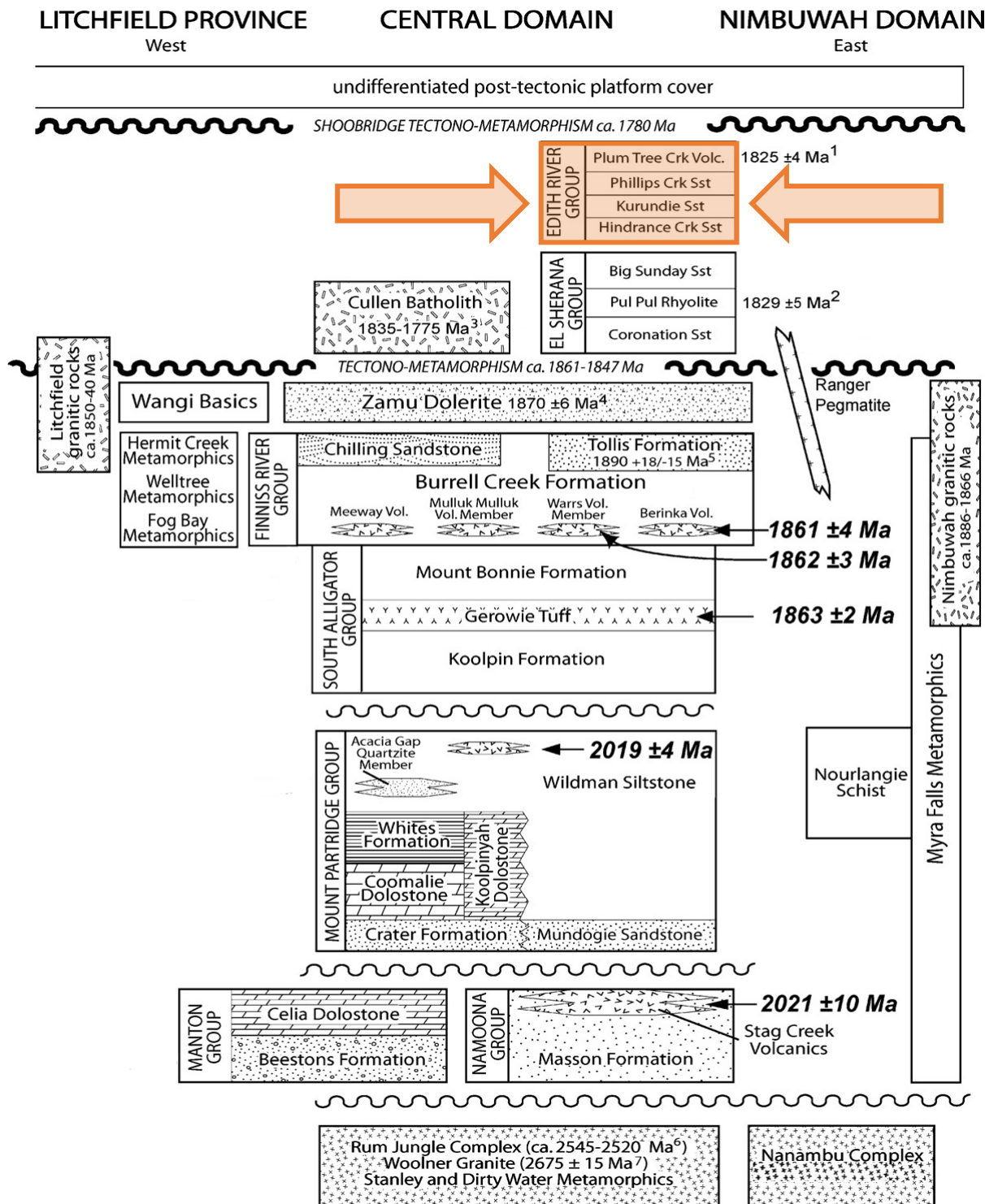
PINE CREEK OROGEN

Figure 5: Simplified stratigraphic log of the Pine Creek Orogen adapted from (Worden, Carson, Scrimgeour, Lally, & Doyle, 2008) showing the major geological regions. The ERG is highlighted in orange. SHRIMP U-Pb zircon data from Worden (2008) is italicised in bold and prior geochronology is indicated in small text at the appropriate stratigraphic unit. (1) SHRIMP zircon extrusion age (Page 1996a); (2) SHRIMP zircon extrusion age (Jagodzinski, 1998); (3) SHRIMP zircon emplacement ages ((Stuart-Smith, 1993); (4) SHRIMP zircon emplacement age (Page, 1996b); (5) SHRIMP zircon upper intercept deposition age (Page & Williams, 1988); (6) SHRIMP zircon emplacement ages (Cross, Claoué-Long, Scrimgeour, Ahmad, & Kruse, 2005); (7) SHRIMP zircon emplacement age (McAndrew, Williams, & Compston, 1985).

Grace Creek Granite

The Grace Creek Granite (GCG) is located north-east of the ERG. The GCG is red, very fine to medium grained, with phenocrysts of feldspar and chloritized hornblende. It correlates with the PTV rhyolites, with grainsize and groundmass distinguishing them. The GCG shows concentric zoning, and is coarsest near the center (Needham & Stuart-Smith, 1985). This granite has a crystallisation age of 1863 ±5Ma (Page, 1996c), giving it a similar age to that of the PTV. The granite is almost completely surrounded by the PTV ignimbrite and lies coincident with the intersection of the ENE-WSW and NW-SE faults which control the shape of the Edith Falls, Mt Callanan and Birdie Creek Basins (Needham et al., 1988). It has been suggested that the GCG coincides with the volcanic center of the PTV and may be the intrusive remnants of the magma chamber (Needham et al., 1988).

McArthur Basin

The McArthur Basin overlies the Pine Creek Orogen. The oldest formation of the Northwest McArthur Basin is the Katherine River Group- which is comprised mostly of sandstone with interspersed conglomerates, and volcanics at the top (Needham & Stuart-Smith, 1985). The Katherine River Group disconformably overlies the ERG in all three basins (Needham & Stuart-Smith, 1985). The basal Kombolgie Subgroup comprises fluvial sandstone and volcanic units overlying the Edith River Group. The lowermost Mamadawerre Sandstone is a fluvial trough cross-bedded sandstone (Carson, Brakel, & Haines, 1999). The Katherine River group above the Kombolgie Subgroup is comprised of sediments that suggest a fluvial-shallow marine transition.

The age of the PTV overlaps with the age of the Bickerton Rhyolite in the Groote Eylandt Group's Bustard Subgroup (1814 ±8 Ma; (Pietsch, Rawlings, Haines, & Page, 1997)), suggesting possible correlation between these volcanics. The Bustard Subgroup is primarily

rhyolitic volcanics with interbedded sandstones- much like the PTV- supporting this possible correlation.

METHODS

Sample Collection

Samples were collected from localities around the Katherine- Pine Creek region, NT. Drill core samples were collected from the NTGS core library in Darwin (details on drill core sampled in Appendix B). The samples are mafic and felsic volcanics, with one sample of granite collected as a representative of basement composition.

Whole Rock Geochemistry

Samples were milled at The University of Adelaide using a tungsten carbide mill head. Whole rock geochemistry was obtained for all 50 samples via XRF, ICP-MS and ICP-OES by Bureau Veritas (geochemical data in Appendix C). W was eliminated from analyses due to mill contamination.

Radiogenic Isotope Geochemistry

To investigate the source of the PTV, six samples were chosen for Nd-Sm-Sr radiogenic isotope analysis. These samples were chosen due to collectively representing the overall mafic-felsic trend of the suite. Analysis was undertaken at The University of Adelaide under the supervision of David Bruce. Samples were prepared via standard open acid digestion methods using hydrochloric (HCl), nitric (HNO_3) and hydrofluoric (HF) acids. Samples were spiked with a solution of $^{150}Sm/^{147}Nd$. 2mL of 15M HNO_3 and 4mL of 28M HF was added to digest the samples. One sample- due to the presence of zircons- the standard (Granite G2) and the blank were placed in Teflon 'bombs', with the remaining five samples placed in Teflon vials. The bombs were placed in metal jackets and oven-heated at 200˚C for 4 days then

evaporated until dry. 6mL of 6M HCl was added and the bombs were placed back in the

jackets and in the oven at 200˚C overnight. The vials underwent a similar procedure, instead

heated on a hotplate at 140˚C for 2 days and evaporated, then refilled with the same volume

of HNO_3 and HF for another 2 days before 6mL 6M HCl was added. Nd, Sm and Sr were

extracted via column chromatography. Isotope ratios were measured using an Isotopx

Phoenix Thermal Ionisation Mass Spectrometer. The international neodymium standard JNdi-

1 returned a mean value of 0.512081±0.000014. The blank showed negligible Nd and Sm,

and anomalously high Sr. When calculating εNd values, an age of 1825 Ma was used, as this

is the approximate crystallisation age for this suite (isotope data in Appendix D).

Analysis

The IgPet software (Carr, 2002) was used to plot geochemical data on Harker Diagrams,

tectonic discrimination diagrams and REE Spidergrams. Rhyolite-MELTS (Ghiorso &

Gualda, 2015; Gualda, Ghiorso, Lemons, & Carley, 2012) was used to determine a model of

liquid line of descent using PT18-013 as it is the most primitive basalt that conformed to

trends in the suite (settings used and extended methods in Appendix E).

OBSERVATIONS AND RESULTS

Geochemical Analysis

The PTV suite shows a bimodal distribution of felsic-mafic volcanism that positively

correlates alkalis with silica. Two distinct clusters are evident, one in the basalt field of the

mafic end-member and a second dacite-rhyolite cluster at the felsic end-member (Figure 6).

The bimodality of this suite is highlighted by the presence of a Daly Gap (Daly, 1925) - a

lack of substantial preserved intermediate samples- between 57-62% SiO_2 (Figure 6). The

volumetric representation of samples is skewed towards dacite-rhyolite compositions.

Chondrite normalised REE patterns show similar HREE patterns for the mafic and felsic samples (Figure 7). The felsic samples are more enriched in LREEs and show more pronounced Eu anomalies than the mafics. The mafics show somewhat flatter trends, with a less pronounced Eu anomaly.
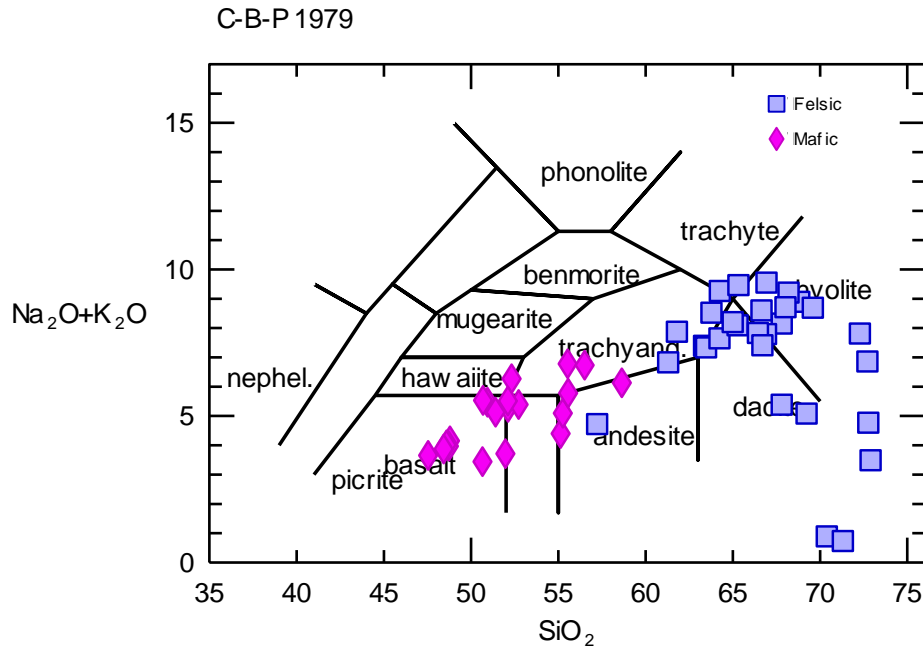
Figure 6: Total Alkali-Silica (TAS) diagram for the collected PTV samples. Mafic samples are marked with pink diamonds and felsic samples are marked with blue squares.
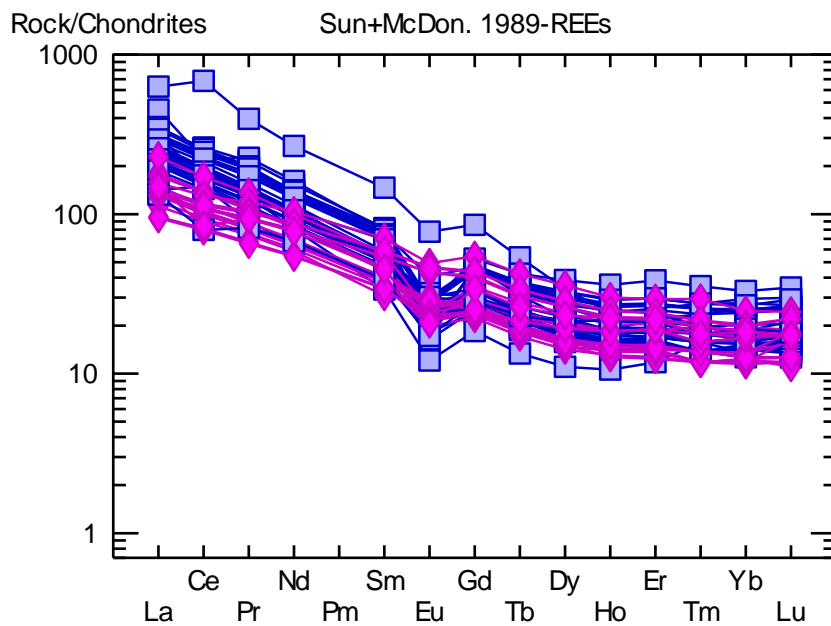
Figure 7: Chondrite normalised REE diagram of the PTV samples normalised to chondrite. Mafic samples are marked with pink diamonds, felsic samples are marked with blue squares.

Some of the analysed felsic samples show a depletion of Na_2O and CaO (Figure 8) as a result of post-emplacement alteration. The alteration in these samples is possibly due to devitrification of glass and breakdown of feldspars leading to a leakage of alkalis out of the rock over geological time.
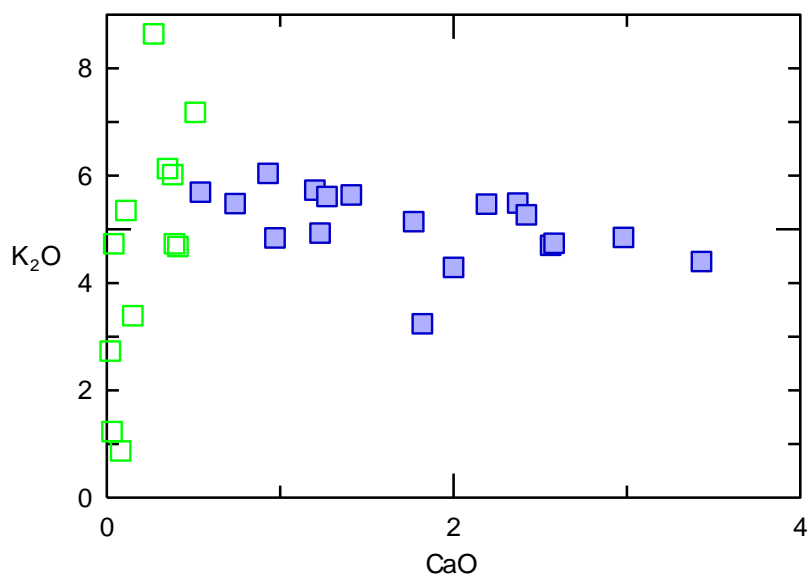
Figure 8: CaO vs K₂O plot for the PTV rhyolites showing alteration in the rhyolites of the suite. Altered samples are marked as green squares, non-altered samples are blue squares.

Petrography

Four samples were examined in thin section: basalts (PT17-001 and PT17-021), rhyolite (PT17-002) and a rhyolite ignimbrite (PT17-015). These were chosen to highlight the change in mineralogy between the two primary melt compositions.

PT17-001 is a fresh, basalt with an intersertal texture and groundmass of mostly rounded grains of glass, magnetite, chlorite, and pyroxenes. Phenocrysts of olivine replaced by chlorite and zoned plagioclase are present. Biotite is present as vug infill (Figure 9.a). Some opaque minerals are included within chlorite, and pyroxene is observed surrounding larger opaque grains.

The rhyolite sample (PT17-002) has a flow texture and comprised mostly of a mostly recrystallised glassy groundmass. Blocky and tabular phenocrysts of plagioclase are common, some of which show alteration by a later melt stage (Figure 9.b). The plagioclase grain in the photomicrograph is a sericitized 3-zoned plagioclase grain. Phenocrysts of chlorite and biotite are also common.

The rhyolite ignimbrite sample (PT17-015) is largely composed of a trachytic glass groundmass (Figure 9.c). The sample has numerous glass-rimmed veins with quartz infill. Equant and blocky phenocrysts of plagioclase, chlorite and biotite are common with minor phenocrysts of olivine and titanite. Titanite is also observed intergrown with chlorite phenocrysts.

The second basalt sample (PT17-021) has an intergranular, mostly bladed groundmass of plagioclase overgrown by rounded clinopyroxene and magnetite grains (Figure 9.d). Plagioclase phenocrysts are abundant, some of which contain clinopyroxene and chlorite inclusions. Some plagioclase phenocrysts show evidence of alteration, where some grains show sericitization. The sample includes large dirty looking patches of glass in the groundmass.
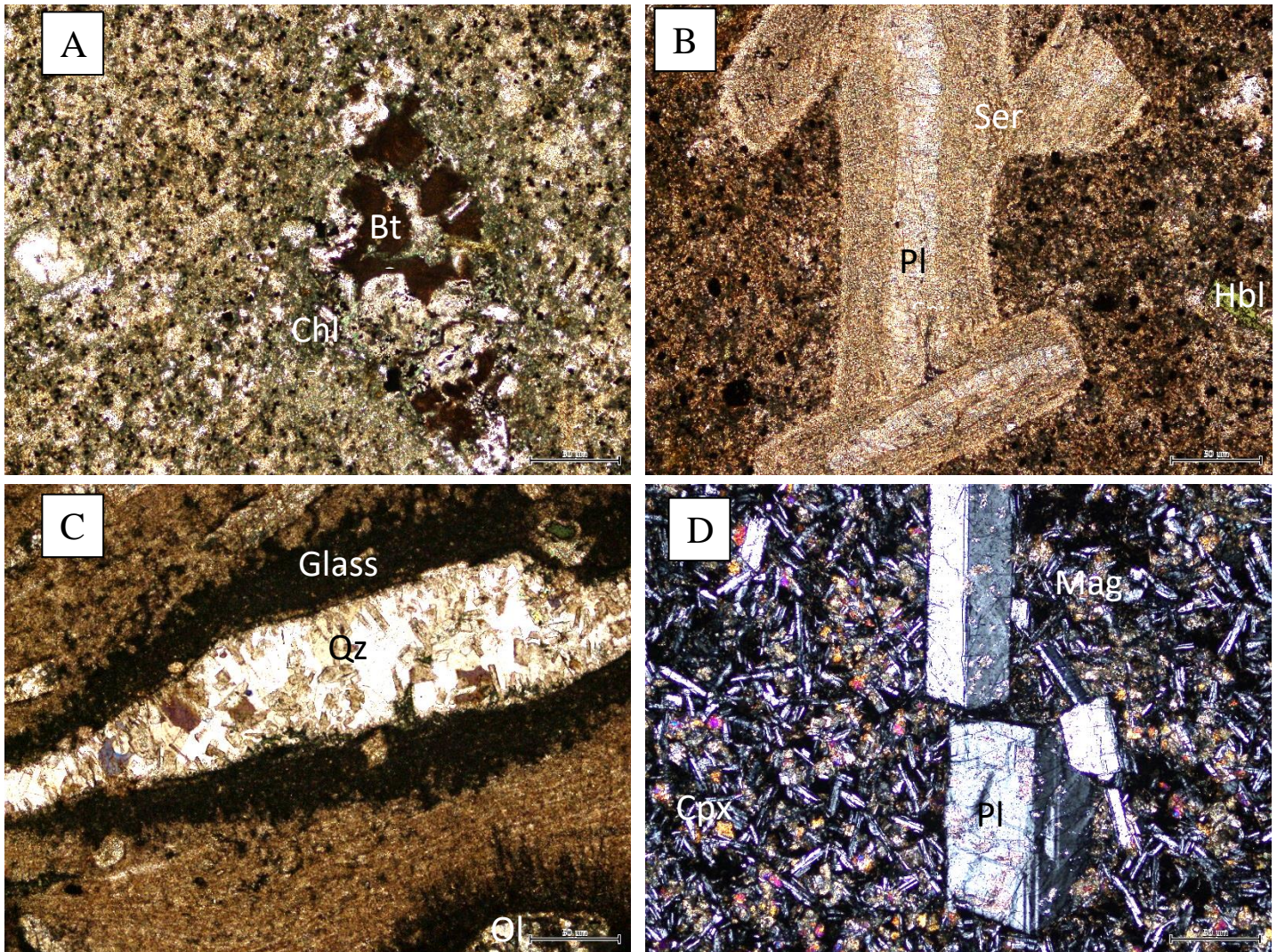
Figure 9: Photomicrographs of each sample studied via optical petrography. Note the scale for each photomicrograph is 50 microns. (A) PT17-001: basalt. Mostly magnetite, glass and clinopyroxene groundmass. Plagioclase phenocrysts replaced by biotite and surrounded by chlorite. (B) PT17-002: rhyolite. Phenocrysts of zoned plagioclase replaced by sericite, and a phenocryst of hornblende. Groundmass is glass with intergrown magnetite. (C) PT17-015: rhyolite ignimbrite. Plagioclase, olivine and quartz phenocrysts. Groundmass is trachytic glass. Some veining with quartz infill and glass rims. (D) PT17-021: basalt. Phenocrysts of plagioclase. Groundmass consists of bladed plagioclase grains and glass overgrown by round clinopyroxene grains. Magnetite exists as rounded grains in the groundmass.

DISCUSSION

Petrogenesis

FRACTIONAL CRYSTALLISATION

Rhyolite-MELTS (Ghiorso & Gualda, 2015; Gualda et al., 2012) modelling of pure

fractionation shows mixed outcomes when compared to the true values of the PTV suite

(Figure 10). The most primitive basalt was used as a starting composition for the purpose of

modelling. Spacing of the modelled points reflect the amount of change of the element for a

constant rate of cooling. The MELTS liquid line of descent plots similarly to the most

primitive compositions of the suite, with Al_2O_3 increasing with SiO_2. At -~52% SiO_2, there is

an inflection towards decreasing Al_2O_3 concentrations. This is similar to the samples except it

occurs at a lower SiO_2 concentration. The modelling plots perfectly along the same

decreasing trend for MgO with separated points in the observed Daly Gap. When compared

with the true FeO concentrations, melt modelling plots with a loose similarity for the basalts

and a strong similarity for the rhyolites, with a dense line of data points at the same

concentration as the samples with >60% SiO_2. The model for Na_2O vs SiO_2 also fits the data

well with strong correlation with the sample compositions. This melt modelling suggests that

petrogenesis was primarily driven by fractional crystallisation with lesser crustal

contamination.
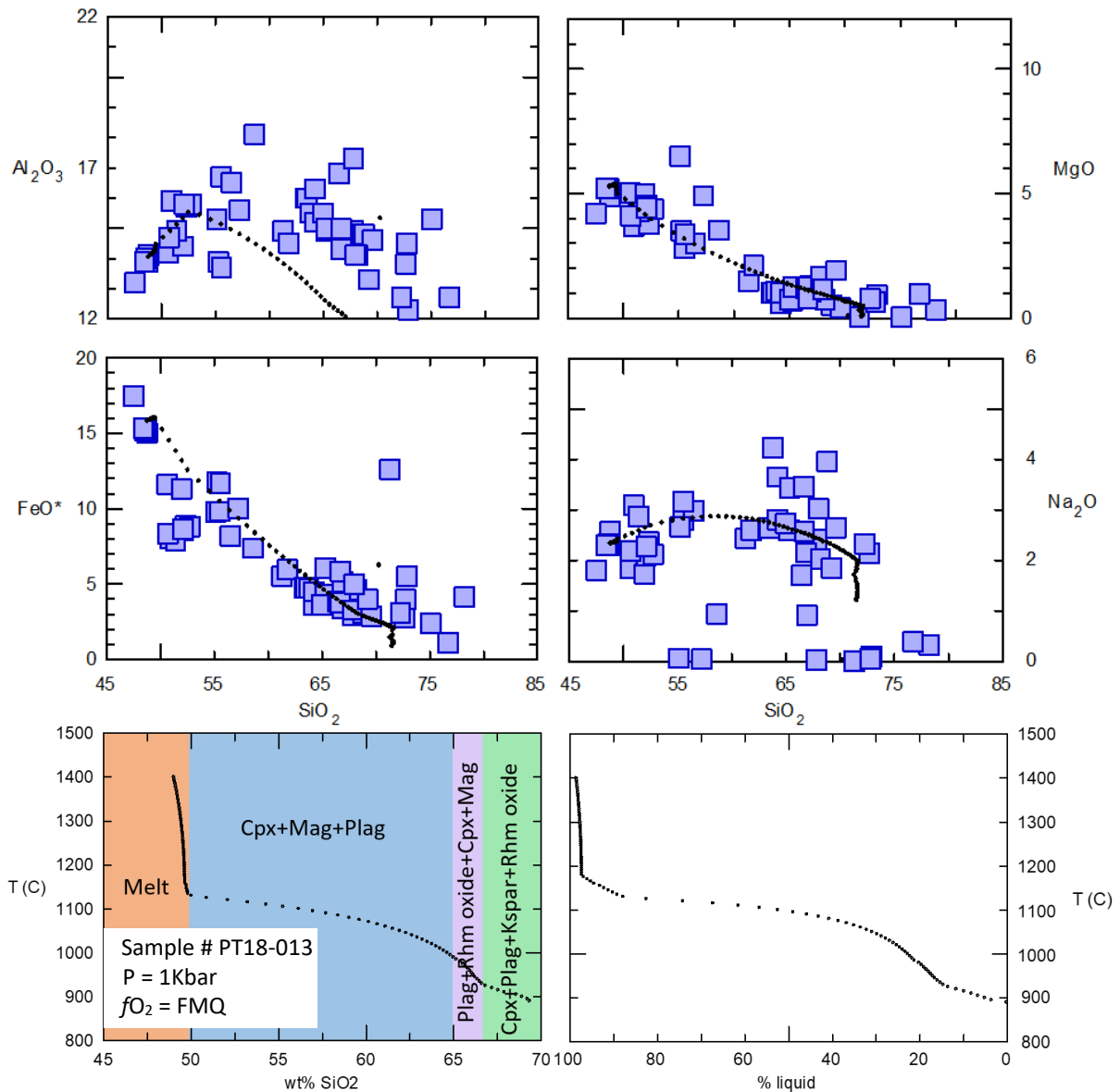
Figure 10: Rhyolite-MELTS liquid line of descent calculated at 1000 bars compared to the actual data of the PTV suite for a selection of major element oxides. T (°C) vs SiO₂ (wt%) with MELTS calculated mineral assemblages included. T (°C) vs % liquid remaining also shown.

The PTV samples were plotted on major element diagrams alongside compositions of likely minerals at 5%, 10% and 20% crystallisation to determine the mineral assemblages that formed during crystallisation (Figure 11). On a CaO vs SiO₂ diagram, the basalt shows correlation with clinopyroxene and magnetite with no correlation minerals for the rhyolites. The basalt on a SiO₂ vs MgO diagram shows correlation with plagioclase, clinopyroxene, orthopyroxene and magnetite. The rhyolite shows correlation with plagioclase and sanidine.

The trend for the PTV basalts for alkalis vs SiO_2 shows an intersection between magnetite and clinopyroxene with plagioclase, sanidine and biotite for rhyolites. The basalts on an Al_2O_3 vs SiO_2 diagram show correlation with plagioclase and clinopyroxene, the rhyolite shows correlation with biotite, clinopyroxene and orthopyroxene. From these diagrams combined with petrographic observations (Figure 9), a mineral assemblage of plagioclase + clinopyroxene → magnetite + plagioclase → sanidine + plagioclase can be identified in this suite.
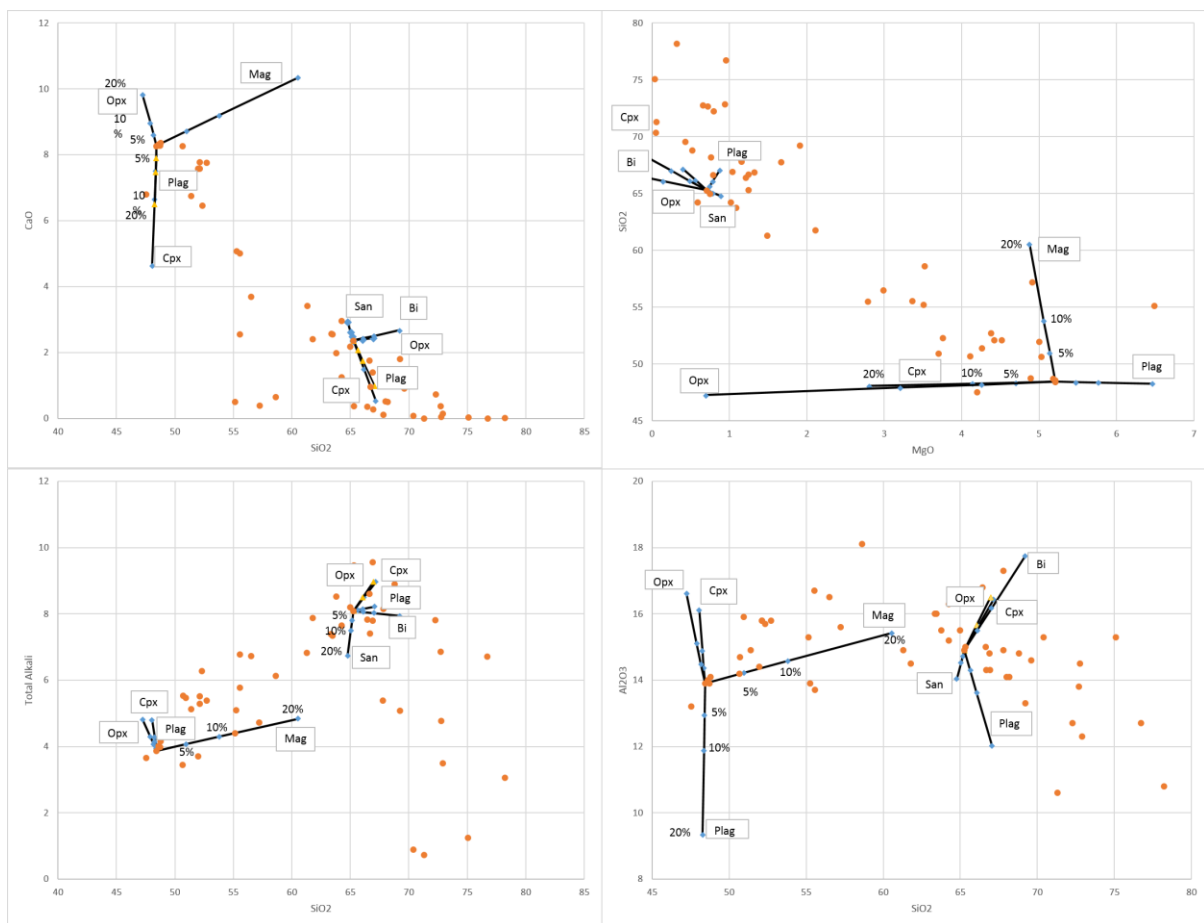
Figure 11: Major element oxide plots of the PTV samples with mineral assemblage vectors for a representative basalt (PT18-013) and rhyolite (PT17-017). Modelled mineral vectors were calculated at 5%, 10% and 15% crystallisation. Plag= Plagioclase, Bi= Biotite, Cpx= Clinopyroxene, Opx= Orthopyroxene, San= Sanidine.

ASSIMILATION FRACTIONAL CRYSTALLISATION

The Rhyolite-MELTs program depicts a trend of pure fractional crystallisation that adequately fits the observed compositions in the PTV suite (Figure 10). The modelled best fit pressure suggests that fractional crystallisation began at 1000 bars. This shallow fractional crystallisation supports the continental rifting model, as these settings involve lithospheric thinning due to mantle upwelling (T. Ahmad, Longjam, Fouzdar, Bickle, & Chapman, 2009; McKenzie & Bickle, 1988).

The isotope data for the PTV supports a crustal contaminant. Analysed PTV samples possess negative $\varepsilon Nd(t)$, similar to the PCO basement (Figure 14). The PCO basement shows two distinct groups, one with similar εNd to the PTV, and one with much more negative. As the PTV is very negative compared to depleted mantle, it is likely there has been some extent of assimilation of continental crust; either a significant volume of less negative, or a smaller volume of more negative crust.

It is likely that the PTV is the result of an AFC process. During ascent the melt assimilated lower continental crust, as modelled in Figure 12. The modelled AFC trends for average lower, middle, upper and bulk continental crust show trends of AFC suggesting the lower continental crust is the most plausible assimilant. This is supported by literature which states that high heat flow is required to melt continental crust, and that even then only the lower continental crust is melted in significant enough volumes to contaminate a melt (Allen, 2001; Babeyko, Sobolev, Trumbull, Oncken, & Lavier, 2002).

The trends for AFC vs REEs show variation from the observed REE values for the PTV rhyolites (Figure 13). The r value is the ratio of assimilation to fractional crystallisation, where 1= pure fractional crystallisation. The rhyolite LREEs are most similar to r=0.2-0.35. The MREE and HREE patterns are most similar to r=0.6. These combined suggest a

subduction zone trend, which can be explained by crustal contamination. The rhyolite has a more pronounced Eu anomaly, suggesting high plagioclase crystallisation and supported by petrographic observations (Figure 9) (further supporting a contaminated mantle upwelling derived melt rather than a convergent setting). The trends created by the data suggest a genesis of mostly dominated by fractional crystallisation with a small volume of crustal assimilation.
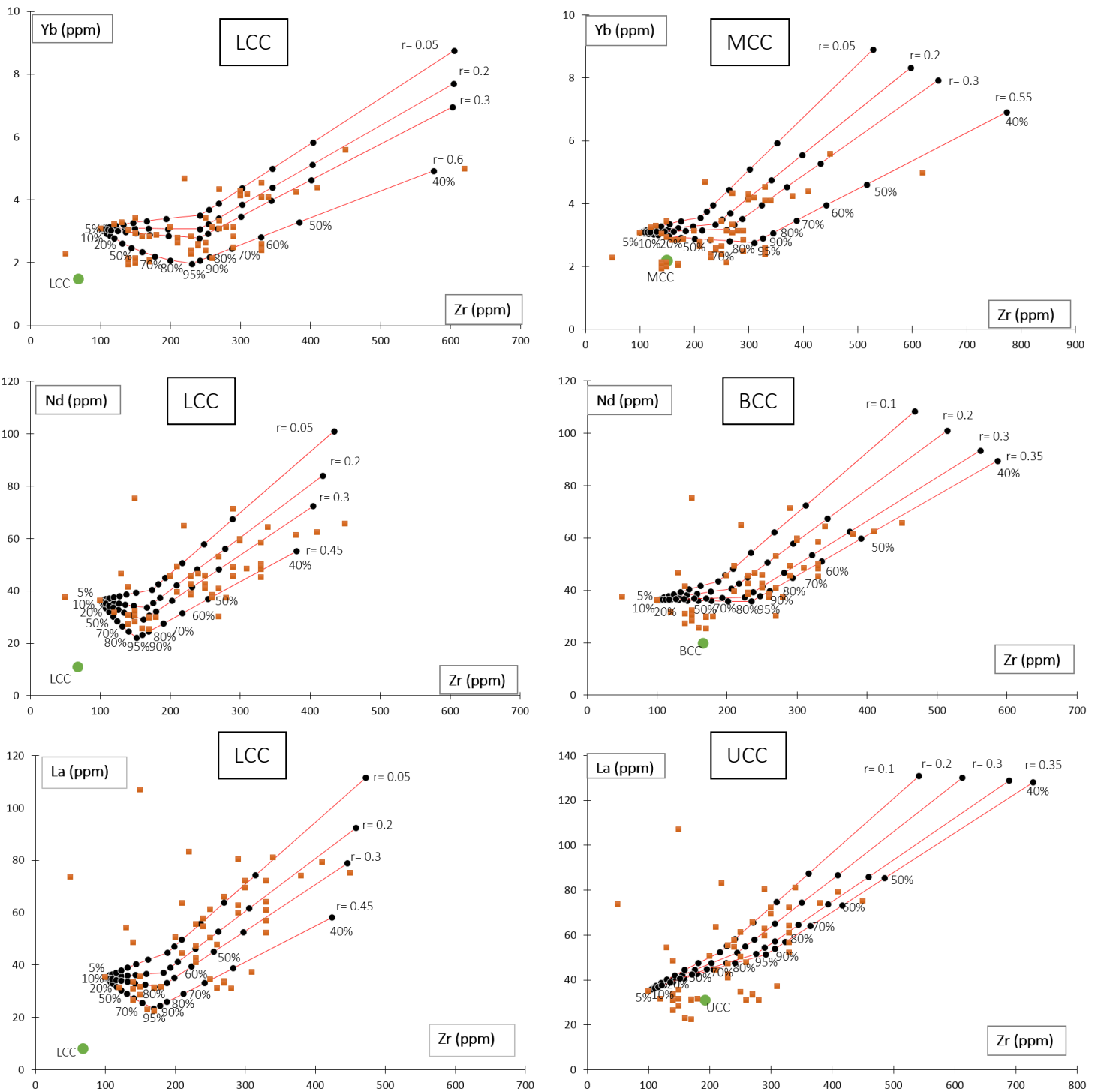
Figure 12: Trace element (Yb, Nd and La (ppm)) vs Zr (ppm) plots showing modelled combined AFC. Orange squares are observed PTV compositions. Black dots are melt percentages, red lines are modelled liquid lines of descent. R values are the ratio of assimilation to fractional crystallisation, where r= 0 is pure fractionation. Green dots are average continental crust values (Rudnick & Gao, 2003). LCC= lower continental crust, MCC= middle continental crust, BCC= bulk continental crust, UCC= upper continental crust. Note labels for 30%, 40% and 60% melt percentage have been removed for clarity.
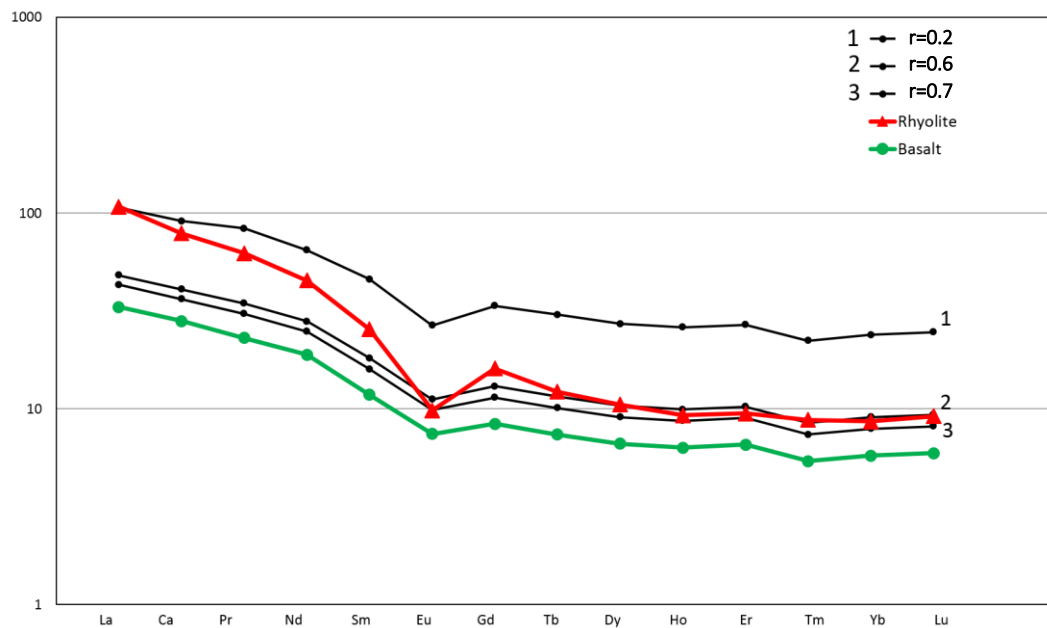
Figure 13: REE diagram of fractional crystallisation trends in the PTV using PT17-020 (green) as a parent melt. Mineral assemblages were used to calculate element fractionation during melt evolution. A representative rhyolite (red) was used to compare model results with a true composition. Mineral assemblage percentages used were: Olivine= 5.00%; Orthopyroxene= 5.00%; Clinopyroxene= 20.00%; Plagioclase= 70.00%; Allanite=0.01%

RADIOGENIC ISOTOPE ANALYSIS

The εNd of the measured PTV samples ranges from -4.93 to -8.9 at 1825Ma (Figure 14). There is no apparent correlation between εNd and rock type. The basement PCO has been divided into two groups; a more primitive group at approximately εNd(1825Ma) -10 and one with approximately εNd(1825Ma) -26. These groups represent the possible contaminants of the PTV which considerably lower the εNd of the suite from approximate depleted mantle εNd at 1825 Ma of +6.

The isotope unmixing plot (Figure 15) shows the volume of crustal assimilant required to reach the εNd observed in the PTV samples. The trend shows that ~15% crustal assimilation is required to reach the evolved PTV εNd signatures observed.

The ratio of radiogenic Sr against SiO_2 shows positive correlation, with the PTV suite plotting along trend from average MORB (Figure 16). The average YSRP basalt plots similarly to the

PTV basalts. When plotted against MgO, a negative correlation is evident with average

MORB plotting along trend of the PTV and average YSRP basalt plotting similarly to the

PTV basalts. This correlation suggests a mantle plume or upwelling sourced melt.
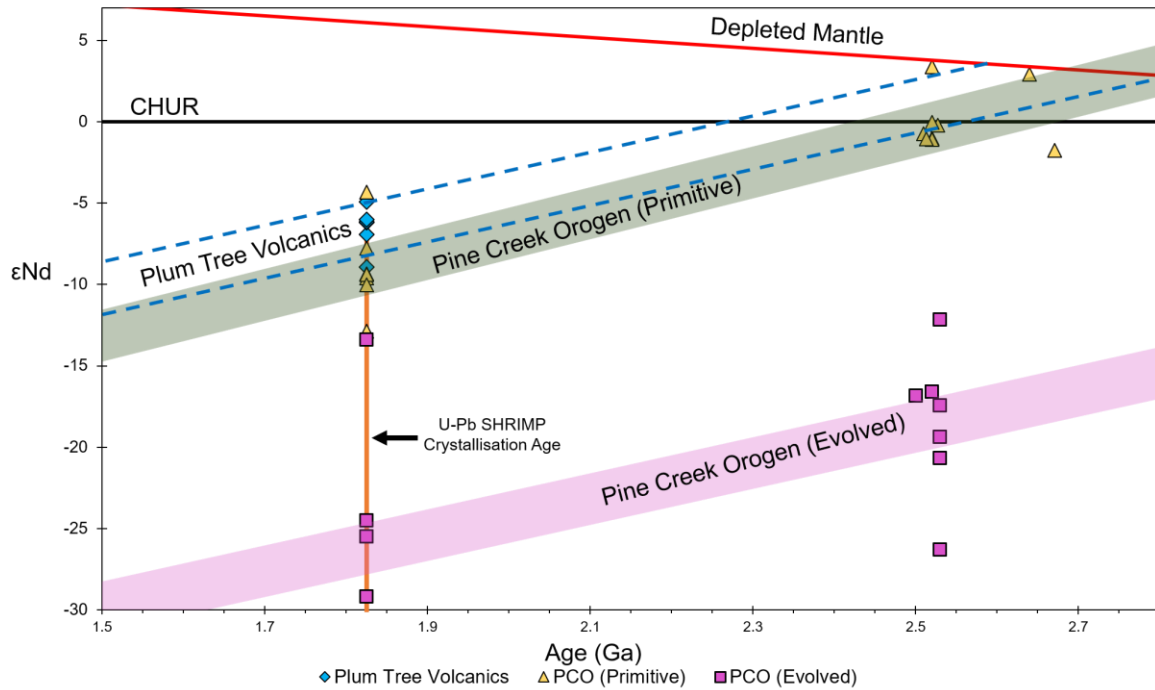
Figure 14: Magmatic age εNd for the PTV against time (Ga). The evolutionary trajectory for the PTV is marked in dotted blue. The Pine Creek Orogen represents the potential crustal contaminant for the PTV melt and has been split into two groups at formation: a primitive group with positive to less negative εNd, and an evolved group with more negative εNd. The evolutionary trajectory of the primitive PCO is shaded green and the evolutionary trajectory of the evolved group is shaded pink. CHUR is marked as a solid black line and Depleted Mantle is marked as a red line. The U-Pb crystallisation age of the PTV is marked by an orange line. Measured PTV isotope ratios are marked with blue diamonds. Primitive and evolved PCO are marked by yellow triangles and pink squares respectively. PCO values were calculated using literature values from (Champion, 2013).
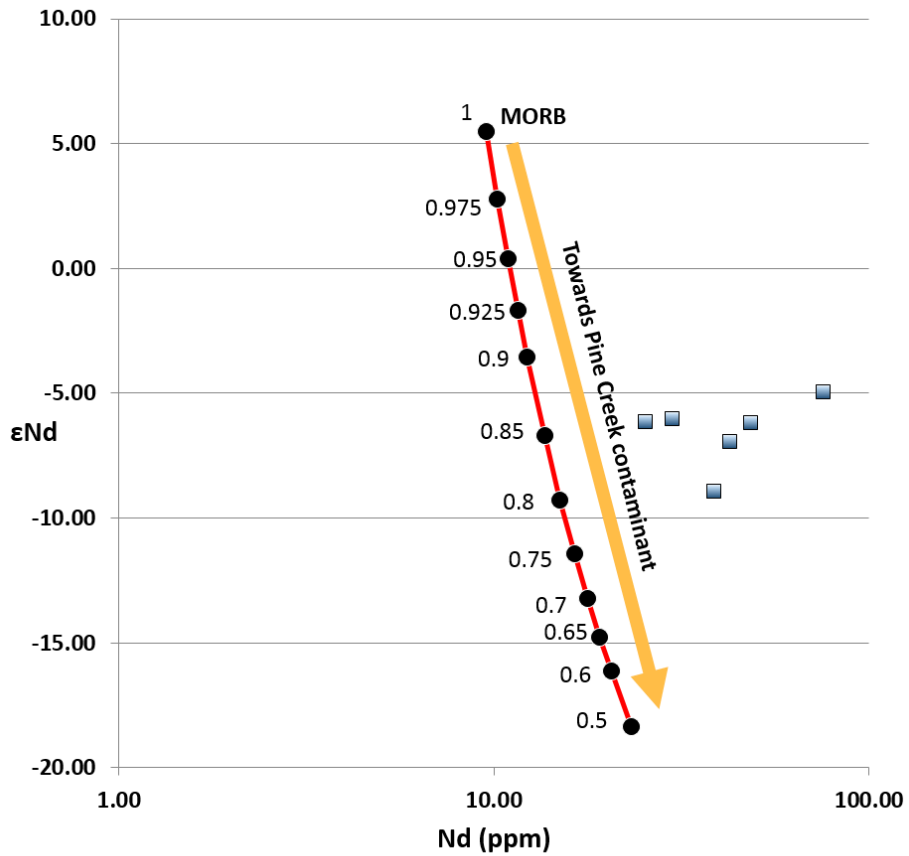
Figure 15: Nd isotope unmixing trend for the PTV samples using average MORB (εNd t=1825Ma) as a starting composition and a sample of evolved PCO as a contaminant. The modelled trend is % melt remaining (numbers next to points on the trend). Blue squares are analysed PTV samples.
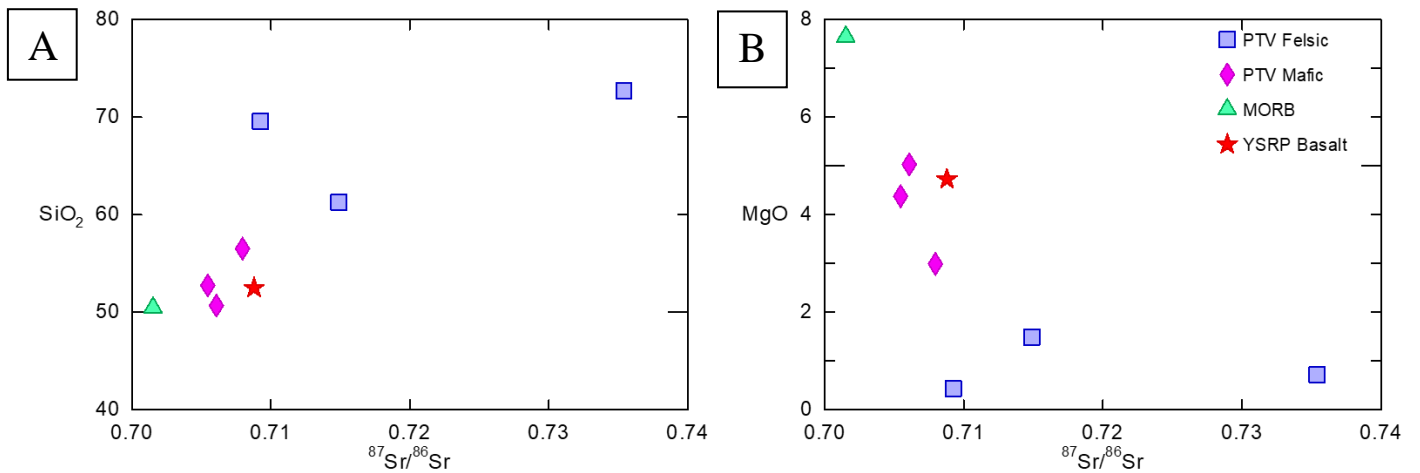
Figure 16: $^{87}Sr/^{86}Sr$ vs major element oxides. (A) Shows radiogenic Sr vs SiO₂. (B) Shows radiogenic Sr vs MgO. Blue squares are PTV felsic samples, pink diamonds are PTV mafic, green triangle is average MORB and red star is average YSRP basalt.

Comparison with volcanic suites of adjacent Proterozoic blocks

When compared with similarly aged volcanic suites, the PTV shows a similar distribution to the volcanics of the Davenport Province, the McArthur Basin, Halls Creek Orogen and the Mount Isa Inlier (Data from GA's OZCHRON Dataset (Champion, Budd, Hazell, & Sedgmen, 2007) (Figure 17). The PCO basement shows similarly depleted concentrations of Na_2O and CaO to some of the PTV samples. The PTV presents similar trends to the volcanics in the Davenport Province and the McArthur Basin (Figure 18). They also show similar trends to the PCO basement.
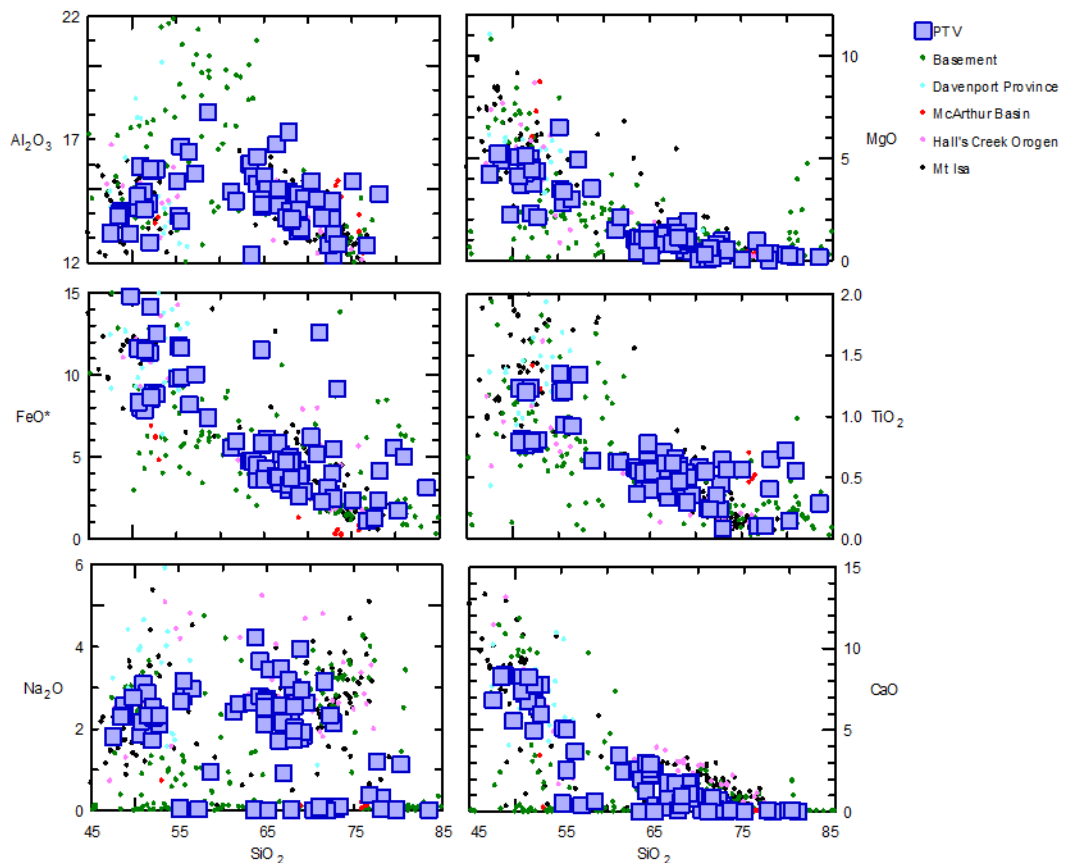
Figure 17: Major element oxides (wt %) against SiO₂ (wt %) for PTV and age synchronous volcanic units in the Davenport Province, McArthur Basin, Hall's Creek Orogen and Mt Isa. Diagrams for K₂O and P₂O₅ have been excluded due to a lack of data on these suites. Pine Creek Orogen included to highlight potential similarities to basement.
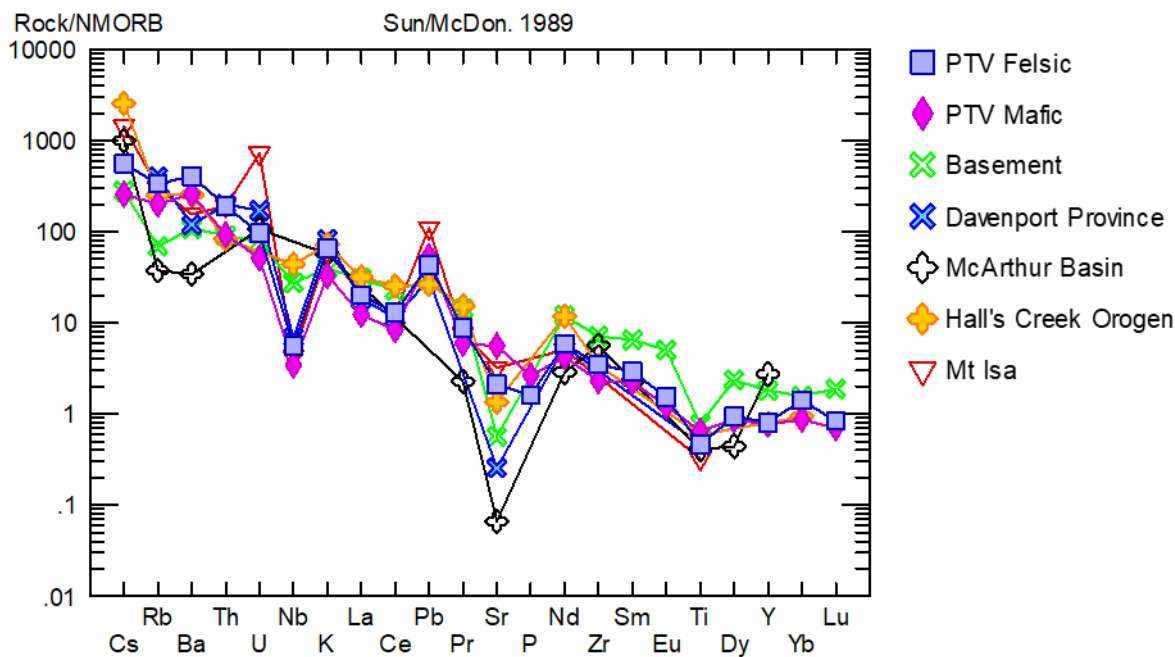
Figure 18: NMORB normalised spidergram showing a selection of samples from the PTV and age synchronous volcanic suites in the Davenport Province, McArthur Basin, Hall's Creek Orogen, Mount Isa Inlier, and the Pine Creek Orogen basement. Normalising values are from Sun and McDonough (1989)

The Bustard Subgroup is part of the lower Groote Eylandt Group of the McArthur Basin. This subgroup, includes the basal Bickerton Rhyolite which has previously been suggested to be a correlative of the PTV (M. Ahmad & Munson, 2013; Rawlings, 1999). The Bickerton Rhyolite has a minimum U-Pb SHRIMP age of 1814 ±8Ma (Pietsch et al., 1997), and therefore overlaps the minimum age of the PTV. These lavas outcrop on Groote Eylandt and shows similar sedimentological and depositional features to the ERG with interbedded sandstone-conglomerate units and a with disconformable relationship with the overlying Alyangula Subgroup (Rawlings, 1999). This correlation is strengthened by comparisons with the major element geochemistry of the two suites (Figure 17). The Groote Eylandt lavas show similar trends to the PTV suite. Despite this, the spider plot pattern of the Bickerton Rhyolite is significantly different to the PTV (shown as the McArthur Basin in Figure 18) with a depletion in Sr and Ba.

The Davenport Province is located south in the Northern Territory, near the town of Tennent Creek. The Ooradidgee Group is part of the mid Davenport Province. It is made up of mostly felsic volcanic units and interbedded sediments (Blake & Page, 1988). This suite has a minimum age of 1816 ±8Ma in the Treasure Volcanics to 1837 ±5Ma in the Epenarra Volcanics (Claoué-Long, Maidment, & Donnellan, 2008). The rhyolite ignimbrite and interbedded sandstone Treasure Volcanics is laterally correlated with the Mia Mia Volcanics in the same group (M. Ahmad & Munson, 2013). This group, combined with the overlying, mostly sandstone Hatches Creek Group has been suggested to be the result of intracontinental rift formation, as evidenced by the fluvial and shallow marine sediments and syn-depositional faulting (Blake & Page, 1988). The major element geochemistry of these volcanics (Figure 17) units show strong similarities to the PTV, albeit with some slightly more enriched samples at <55% SiO_2. The spider plot pattern (Figure 18) is similar to that of the PTV, however with an enrichment in Yb and a depletion in Sr. the geochemical observations combined with stratigraphic similarities suggest possible correlation between these volcanics and the PTV.

The Mt Isa Orogen in western Queensland and contains similar aged volcanic suites to the PTV; the Cliffdale Volcanics and the Fiery Creek Volcanics. The Cliffdale Volcanics are 1870-1850 Ma rhyolite and ignimbrite with interbedded sandstone and andesite layers (Scott et al., 2000). The Fiery Creek Volcanics are a bimodal suite of rhyolite- basalt and interbedded sandstones, much like the PTV. This unit has a maximum age of 1708 ±2 Ma, making it too young to be direct correlative of the PTV (Betts, Lister, & O'Dea, 1998). These units show similar incompatible geochemical trends (Figure 17, Figure 18) to the PTV. Although significantly younger than the PTV, these suites have very similar geological context and may result from the same processes.

The Halls Creek Orogen is located in the Kimberley Region of Western Australia. This Orogen contains similarly aged volcanic units to the PTV; the 1855 Ma Whitewater Volcanics (Tyler, Page, & Griffin, 1999) and the 1845-1840 Ma Koongie Park Formation (Tyler, Hocking, & Haines, 2012). The Whitewater Volcanics are felsic volcanics while the Koongie Park Formation is mafic-felsic volcanics and sedimentary units deposited during rifting (Tyler et al., 2012). The major element geochemistry of these units shows similarities to the PTV, with bimodal distribution of compositions (Figure 17). The REE patterns of these units shows strong similarities to the PTV, with similar trends to the PTV mafic samples (Figure 18). Despite these similarities, these volcanics are slightly too old to be correlatives of the PTV. Further geochemical, isotopic and stratigraphic analyses of these age synchronous suites is required in order to make a definitive conclusion on their relationships with the PTV.

It is apparent that correlatives of the PTV exist in other Proterozoic blocks in Australia. Similar time intervals of formation and bimodal volcanism in terrestrial settings with fluvial sandstones and conglomerates support correlation between Palaeoproterozoic volcanic suites in the McArthur Basin, Davenport Province, Mt Isa Orogen and Halls Creek Orogen.

Tectonic Provenance

IDENTIFYING MELT SOURCES

Basalts are more direct reflections of their sources than their associated rhyolitic derivatives and are thus better petro-tectonic indicators (Wilson, 1989). Major element compositions are less useful than minor and trace element compositions for determining melt source as they vary only slightly as melt fraction increases and show less change across tectonic settings while trace and minor elements can show distinct signatures for each setting (Sigurdsson, Houghton, McNutt, Rymer, & Stix, 2015).

TECTONIC SETTINGS

Bimodal volcanic suites possess both mafic and felsic rocks with no or few associated intermediates. They are observed in a variety of tectonic settings. The most common of these is hotspots and intraplate continental rift settings, however they can also occur in convergent settings.

Bimodal hotspot volcanics have a distinct enrichment of incompatible elements (such as Cs, Rb, Ba, Nb, Th, U, K and LREEs), which closely resembles a mantle source (Meschede, 1986). An example of this is the Yellowstone Snake River Plain (YSRP) rhyolite. Based on the radiogenic isotopes of Sr, Nd, Pb, and Hf, this rhyolite is derived from AFC processes (Szymanowski et al., 2015). Table 1 shows the similarities and difference between basalts of varying tectonic settings.

	Plate Margin		Within Plate	
Tectonic Setting	Convergent (destructive)	Divergent (constructive)	Intra-oceanic	Intra-continental
Volcanic Feature	Island arcs, active continental margins	Mid-ocean ridge, back-arc spreading centres	Oceanic islands	Continental rift zones, continental flood basalts provinces
Characteristic Magma Series	Tholeiitic Calc-alkaline Alkaline	Tholeiitic - -	Tholeiitic - Alkaline	Tholeiitic - Alkaline
SiO$_2$ Range	Basalts and differentiates	basalts	Basalts and differentiates	Basalts and differentiates

Table 1: Characteristic magma series associated with specific tectonic settings (Wilson, 1989)

In convergent settings, mafic melts form as a result of flux melting, where volatiles are added to the mantle wedge from the subducting slab (Ulmer, 2001) and differentiation follows a wet and oxidised path (Bachmann & Bergantz, 2008). Arc basalts are unique in that they have high abundances of LILEs (Large Ion Lithophile Elements), such as K, Rb, Ba and Sr, and distinct negative Nb and Ta anomalies (Ryerson & Watson, 1987; Sigurdsson et al., 2015).

Continental rifting occurs when the lithosphere is thinned due to a mantle plume or asthenospheric upwelling. Modern rift settings are characterised by alkali rich mafics and their evolved derivatives (Sigurdsson et al., 2015). Volcanics formed in these settings have unique isotope signatures that differentiate them from volcanics sourced from other settings. Ti, Zr and Y are relatively depleted in these settings compared to other continental volcanic settings, representing primitive, mantle derived melts (Floyd & Winchester, 1975).

Basalt tectonic discrimination diagrams play a significant role in determining melt source. These diagrams plot elements that are incompatible in different tectonic settings. Trace elements are used to determine tectonic settings. Not all trace elements are useful for this; some elements (eg Al and Ga) show little variation between magma types and muddy discrimination diagrams; and some pairs of elements such as Ta and Nb have such similar geochemical properties to make using them together redundant (Pearce, 1996). The information required to characterise a basalt is determined by eight element variables, the first five of which are the most useful in discrimination (Table 2).

Setting Discriminators	Mantle melting	Mafic FC	Intermediate FC	Subduction	Spinel lherzolite melting	Garnet lherzolite melting	Plagioclase melting
Th or Ce	v. highly incompatible	v. highly incompatible	-	non-conservative	-	-	-
Nb or Ta	v. highly incompatible	v. highly incompatible	-	conservative	-	-	-
Zr or Hf	highly incompatible	highly incompatible	-	conservative	-	-	-
Ti	highly incompatible	highly incompatible	-	conservative	-	-	-
Y, HREE or Sc	-	highly incompatible	-	conservative	highly incompatible	moderately incompatible	-
V	moderately incompatible	moderately incompatible	compatible	conservative	-	-	-
Al or Ga	moderately incompatible	-	-	conservative	-	-	compatible
Cr or Ni	highly compatible	highly compatible	-	conservative	-	-	-

Table 2: Eight element variables used to discriminate basalt tectonic settings. Table created using data from Pearce (1996).

Oceanic basalts are good proxies for continental basalts as they are not contaminated by continental crust. Ocean Island Basalts (OIB) are sourced from hotspots and show variation based on mantle composition source. There are three types of OIB: HIMU, EMI, and EMII. HIMU OIB have low LILE/HFSE (High Field Strength Elements) and La/HFSE ratios that suggest derivation from an ancient, dehydrated subducted slab recycled into the mantle. EMI OIB have higher LILE/HFSE and LREE/HFSE ratios and a relative Ba enrichment. These features are characteristic of subducted oceanic slab with small amounts of entrapped pelagic sediments. EMII OIB have characteristics that suggest derivation from a HIMU source, however LILE/HFSE and LREE/HFSE ratios suggest a component of terrestrial sediments (Weaver, 1991).

ACTIVE VS PASSIVE RIFTING

Intraplate rifting can be divided into two styles: active and passive rifting. Active rifting occurs when the lithosphere is thinned by a mantle plume, and passive rifting where the lithosphere is stretched by asthenospheric upwelling (Figure 19) (Keen, 1985). The primary identifier between these styles is the relative timing of volcanism: doming of the crust and volcanism precede rifting in active rift settings, whereas they succeed rifting in passive settings (Sengör & Burke, 1978).

Due to the relative timing of volcanism in the stratigraphy, volcanism closely following uplift events in the Pine Creek Orogen, and emplacement in shallow rift grabens, it is evident that the PTV is the result of active rifting processes (Worden et al., 2008).
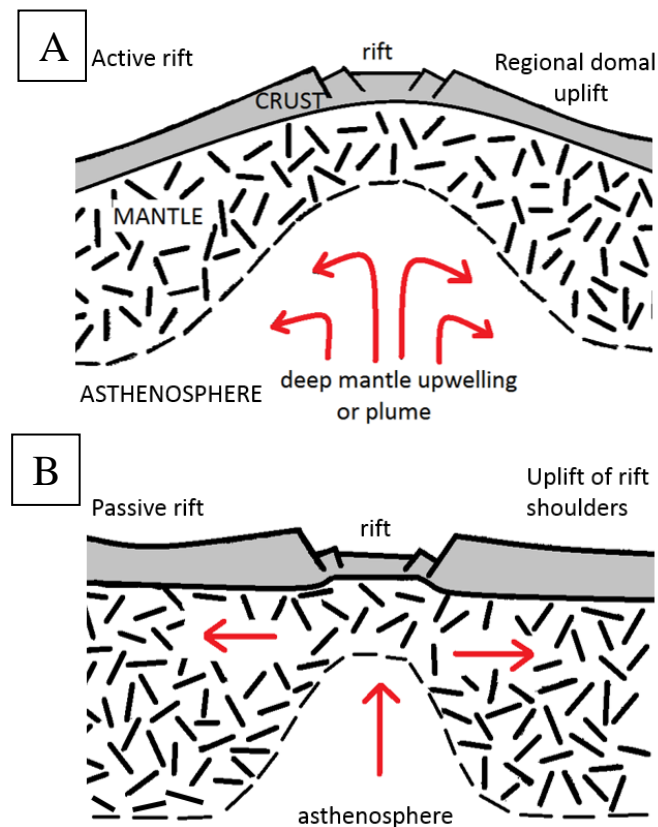
Figure 19: Cartoon of the two rifting models after Keen (1995). (A) Shows active rifting driven by deep mantle upwelling or a mantle plume. (B) shows a model of passive rifting driven by asthenospheric upwelling.

COMPARISON WITH CONTEMPORARY BIMODAL VOLCANIC SUITES

Well understood contemporary bimodal volcanic suites provide useful proxies for understanding the formation of ancient volcanic suites such as the PTV. The YSRP and Karoo LIP suites are two examples of well understood bimodal volcanic suites that can be used this way.

In Harker diagrams, the PTV geochemistry is similar to the YSRP and Karoo LIP suites with strong correlation between the trends of these suites (Figure 20). Of the trends presented in these diagrams, MgO, FeO, TiO, CaO, and P_2O_5 all show decreasing trends with increasing SiO_2, while K_2O shows a consistent trend of enrichment with SiO_2. Al_2O_3 depicts a trend of

enrichment, until an inflection at ~60% SiO_2. Na_2O shows no trend, with a group of data points at around 50% SiO_2 and another at around 70% SiO_2, both at 2-3% Na_2O. It also shows a considerable number of PTV samples plot with ~0.05% Na_2O. CaO similarly shows an array of PTV data that plot at negligible CaO concentration. These low concentrations may be due to alteration, where feldspars are broken down and CaO, Na_2O, and K_2O is released.
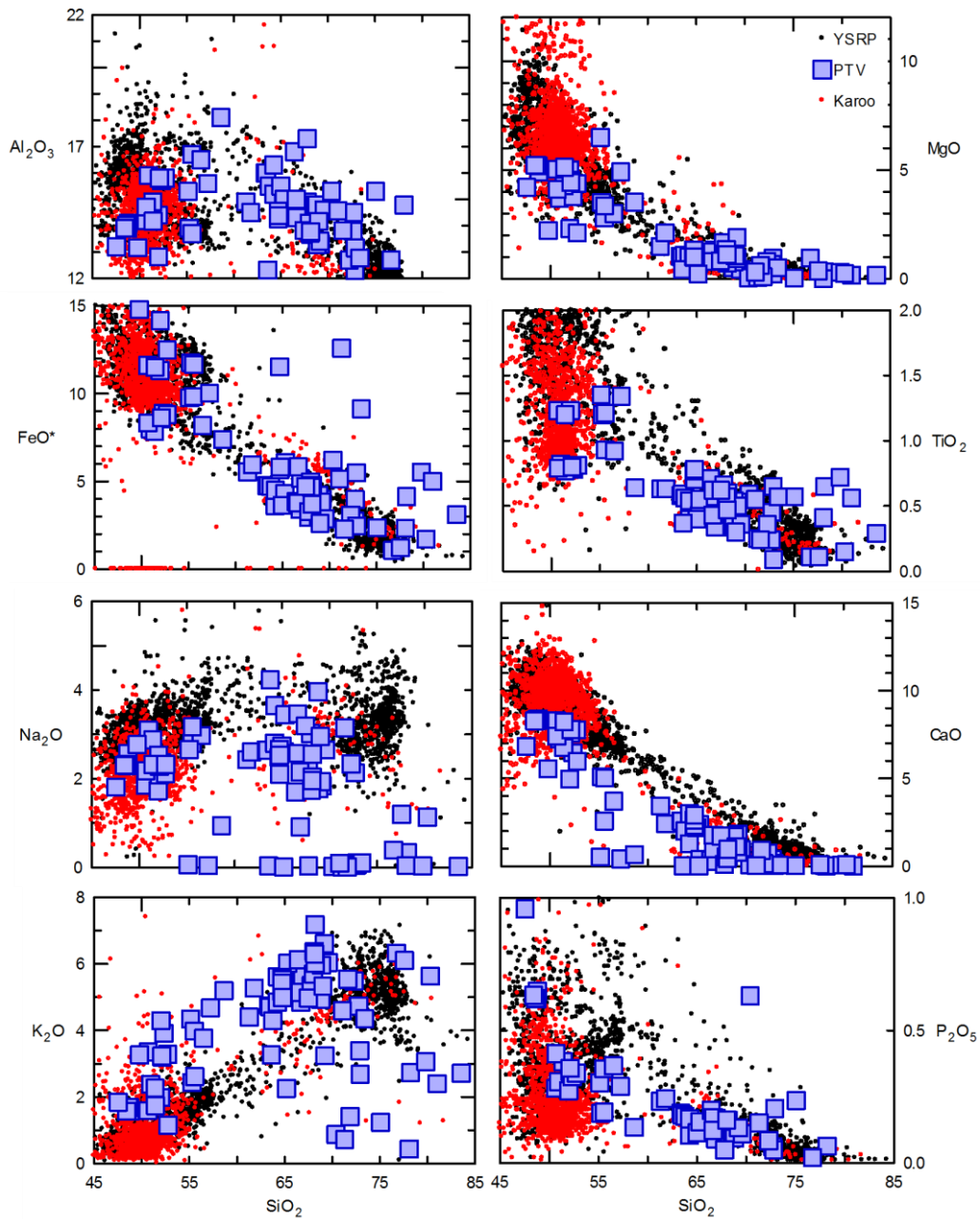
Figure 20: Major element oxides (wt %) vs SiO$_2$ (wt %) diagrams for YSRP, Karoo Large Igneous Province (Szymanowski, Ellis, Bachmann, Guillong, & Phillips) and PTV suites.

A representative sample of the PTV basalt and rhyolite was plotted against a basalt and

rhyolite of the YSRP suite and a basalt of the Karoo LIP on an NMORB normalised

spidergram (Figure 21). LILEs are plotted on the left and HFSEs are plotted on the right of

the figure. The PTV samples present similar trends to the YSRP samples, and to a lesser

extent the Karoo sample. The PTV samples show distinct depletion in Nd and Sr and an

enrichment in Pb.
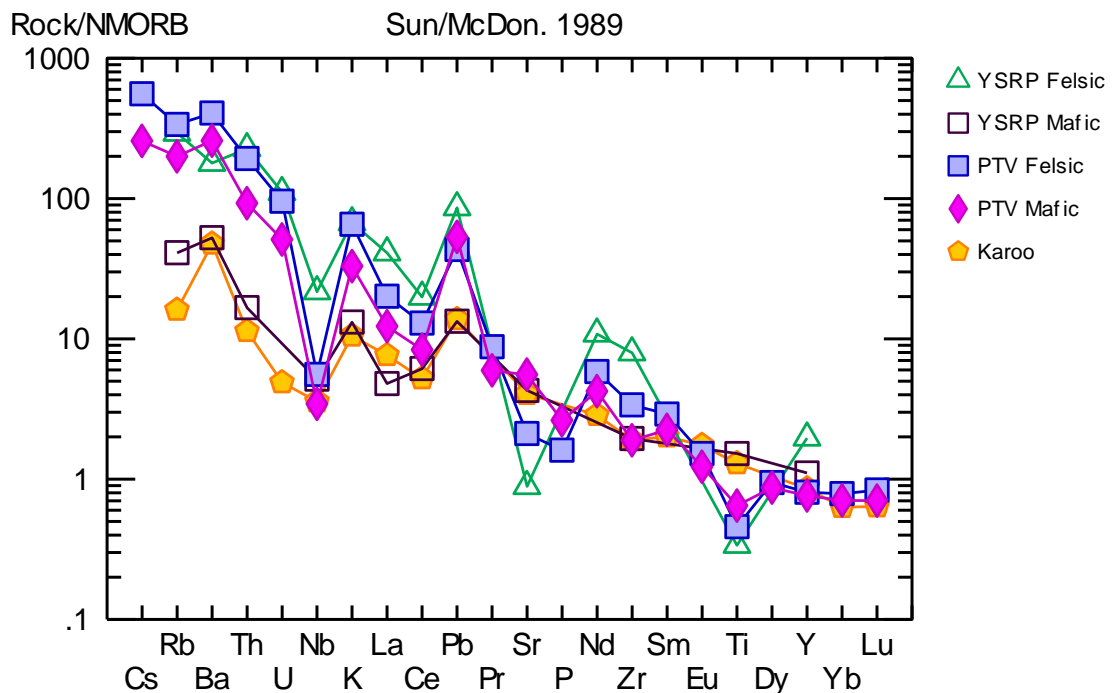
Figure 21: NMORB normalised spidergram showing a selection of samples from the YSRP, Karoo and PTV volcanic suites. Normalising values are from Sun and McDonough (1989)

The YSRP and Karoo LIP possess similar geochemical traits to the PTV. The major element

trends draw strong parallels with one another, both possess distinct bimodality with

somewhat similar Daly Gaps, and increasing and decreasing trends (Figure 20). The YSRP

and Karoo suites both possess far more primitive measured basalts, with <8% MgO

compared to ~6.5% MgO for the most primitive PTV basalt. However, this discrepancy could

be explained by the limited number of collected samples for the PTV compared to the YSRP

and Karoo suites. Despite this, and a few minor differences, such as the PTV having samples of considerably low Na_2O (possibly due to alteration processes) there are vast similarities between these suites. The similarities in major elements for these suites suggest the PTV was formed by a mantle derived parent melt, much like the YSRP hotspot (Szymanowski et al., 2015) and the Karoo intraplate continental rift (Catuneanu et al., 2005).

The REE patterns of these suites present interesting trends (Figure 21). The chosen felsic representative of the YSRP shows similar trends to the PTV felsic samples, with a depletion in Nb, Sr and Ti, and an enrichment in Pb, as expected for felsic volcanics with crustal contamination (Bachmann & Bergantz, 2008). The YSRP and Karoo mafic samples present vastly different trends to the PTV mafic sample with lower overall trends of all REEs, with the exception of a smaller Nb anomaly, a smaller Pb positive anomaly and no Ti anomaly. This can be explained by the more primitive geochemistry of the basalts of these suites. From these major and trace element comparisons, it is plausible that the PTV is the result of a mantle sourced parent melt rather than subducting oceanic slab.

GEOCHEMICAL DISCRIMINATION

Basalt geochemistry plays a significant role in determining the tectonic setting of a parent melt. Continental flood basalts (CFBs) form in a large range of rift related tectonic settings of mantle derived melts and have considerable geochemical variation. Due to their parental variation and the role of crustal contaminants, it is impossible to identify CFBs based on basalt geochemistry alone (Marsh, 1987). This is evident upon inspection of the PTV data on basalt tectonomagmatic discrimination diagrams (Figure 23). On a Zr/4-Nb*2-Y diagram (Figure 23.A) the ambiguous nature of the PTV is clear; the basalts plot indiscriminately and without pronounced definition. Similarly, Figure 23.B shows inconclusive results, albeit with a slightly more defined 'within plate' spread of data. Comparisons can therefore be drawn

between the ambiguous nature of the PTV and CFBs, strengthening the case for a mantle

sourced melt and intraplate continental rifting as the tectonic provenance of the PTV. When

plotted on a Nepheline-Olivine-Quartz normative diagram, the PTV basalts plot as quartz

tholeiites (Figure 22). The parent melt was likely silica saturated when it left the mantle and

was displaced towards silica oversaturation due to assimilation of continental crust.
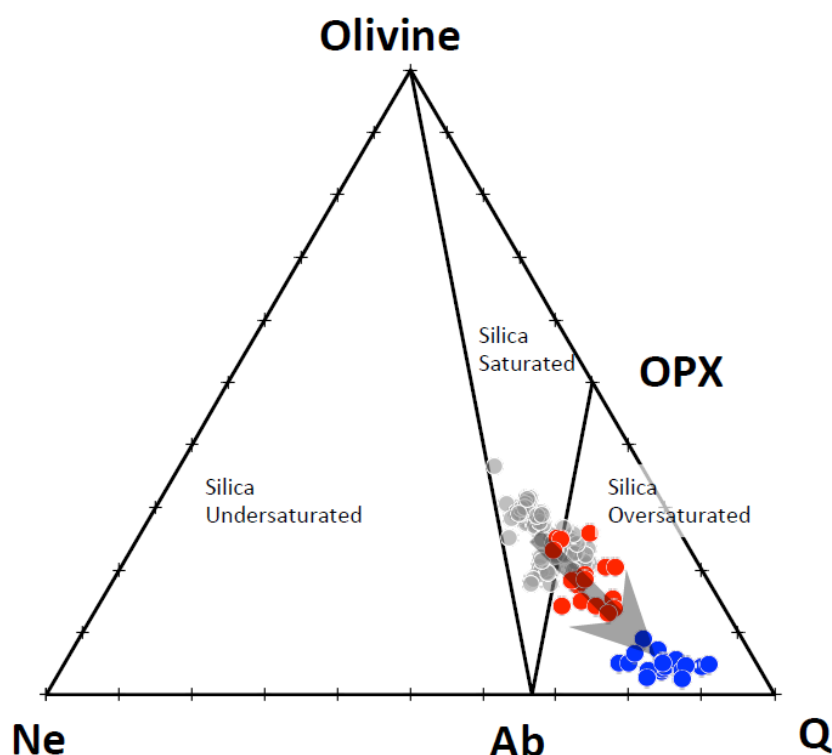
Figure 22: Ne-Ol-Q normative projection of the PTV samples. Red circles are basaltic and andesitic lavas, blue are rhyolites and grey is reference MORB. The arrow indicates direction of fractionation and direction of displacement by continental crustal assimilation.

The PTV basalts depict a scattered distribution on tectonic discrimination diagrams. The

basalts plot ambiguously along the edge of the within-plate tholeiite, alkali and volcanic arc

basalt fields on a Zr/4-Nb*2-Y diagram (Figure 23) making discrimination based solely on

this difficult. Crustal contamination modelling using a PCO granite shows a trend towards

0% Zr/4. However, when plotted on a Zr/Y-Zr discrimination diagram, the basalts show a

distinct cluster in the within-plate basalt field. On this diagram, only a few samples plot

ambiguously along field boundaries or outside of the field area entirely. Modelled crustal

contamination vectors show a decreasing trend to the right of the MORB field.
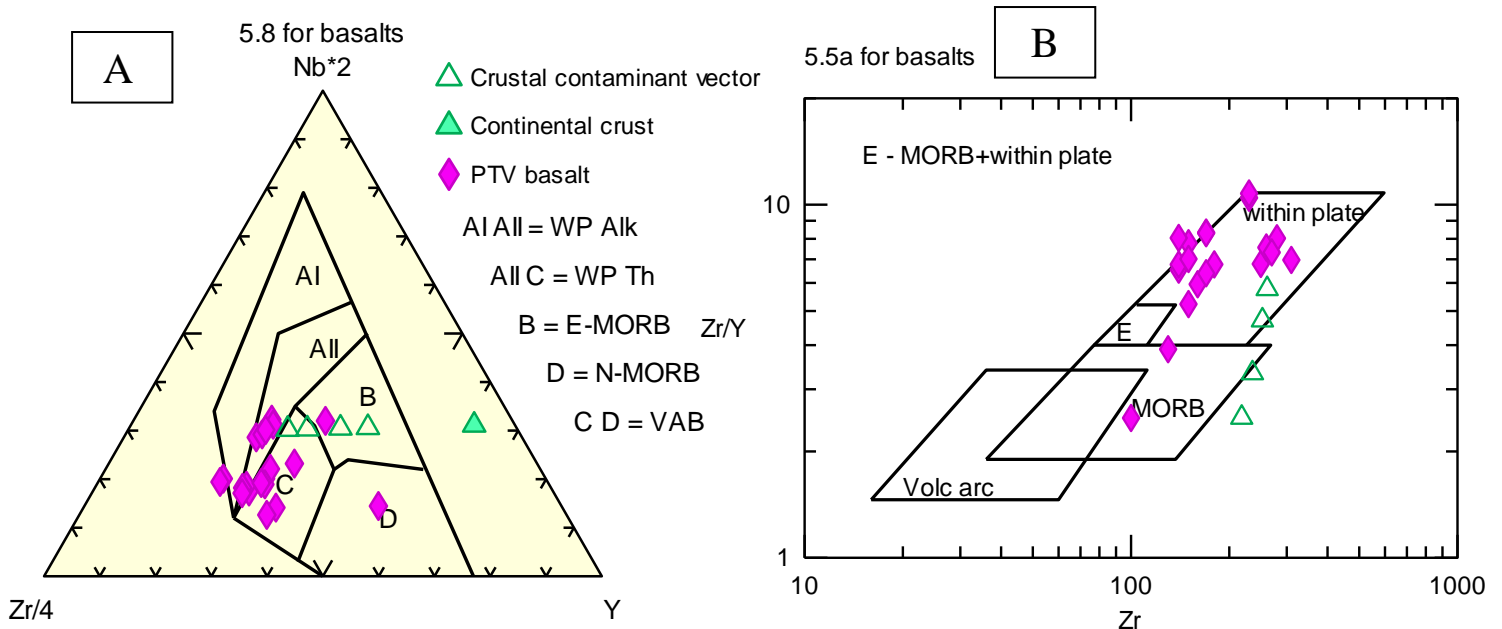
Figure 23: (A) Zr/4-Nb*2-Y basalt tectonic discrimination diagram used for determining the tectonic setting of the PTV basalt's formation. Open triangles are modelled vectors of 5%, 10%, 20% and 30% contamination from a PCO granite. The solid green triangle is the composition of this granite. (B) Zr vs Zr/Y basalt tectonic discrimination diagram used for determining the tectonic setting of PTV Basalt's formation. Open triangles are modelled vectors of 5%, 10%, 20% and 30% contamination from a PCO granite.

CFBs can be divided into two categories: those with ocean-island basalt characteristics, and

those with characteristics that resemble the Lesotho basalt (Marsh, 1987). Lesotho-type

basalts have many crustal characteristics (e.g. high $^{87}Sr/^{86}Sr$, K and Rb) as a result of crustal

contamination. The PTV basalts have a $^{87}Sr/^{86}Sr$ ratio approximately 0.708 (Figure 16);

somewhat higher than expected (Hawkesworth et al., 1979) for basalts, thus categorising

them as Lesotho-type CFBs and implying contamination by a crustal component during

genesis. Bimodal volcanism itself is a significant tool for distinguishing tectonic provenance

of basalts in CFBs (Barberi, Santacroce, & Varet, 1982) as bimodal volcanism is most

commonly associated with rift settings.

Rhyolite discrimination is also significant when determining the petrogenesis of a magmatic suite as they have great variability between subduction and upwelling related magma systems (Bachmann & Bergantz, 2008). Rhyolite REE patterns differ between settings, arc rhyolites typically have lower MREE and HREE patterns with a smaller Eu anomaly due to delayed plagioclase crystallisation and common mineral assemblages (e.g. titanite and amphibole) having low Eu partition coefficients (Bachmann, Dungan, & Bussy, 2005). Mantle sourced rhyolites have enriched MREE and HREEs with a more pronounced Eu anomaly due to the abundant crystallisation of plagioclase. The REE pattern of the PTV suite (Figure 7) suggests a subduction setting, however, it is possible for upwelling rhyolites to have REE patterns that overlap with arc rhyolites and vice versa due to crustal contamination (Bachmann & Bergantz, 2008). This mantle source for the PTV is supported by the mineral assemblages of mostly plagioclase and clinopyroxene in mafic samples and mostly glass in felsic samples (Figure 9, Figure 11).

The oxygen fugacity (fO$_2$) of a volcanic suite is a measure of the system's redox potential at equilibrium and is commonly used to measure the relative ratio of ferrous (Fe^{2+}) to ferric (Fe^{3+}) iron (Aeolus Lee, Leeman, Canil, & Li, 2005). V and Sc were used for this calculation as they have very similar behaviour to one another. They are similarly enriched in the continental crust, arc magmas and MORB relative to primitive mantle, they are both incompatible during the formation of MORB and arc magmas, and are immobile in fluids (Aeolus Lee et al., 2005). They are used in combination in order to reduce the effect of magmatic differentiation processes that may dilute V and Sc concentrations, but not alter their relative proportions. The FMQ (fayalite-magnetite-quartz) buffer is most commonly used to determine fO$_2$, where FMQ -1 represents a melt with Fe almost entirely as ferrous and very little as ferric iron. Conversely, a melt with FMQ +2 has more ferric iron, but still has

mostly ferrous iron. Using the most primitive PTV sample, fO$_2$ was determined as FMQ -1 (Figure 24), suggesting a reduced, primitive parent melt with high ferrous iron. When compared with FMQ of average tectonic settings (Evans, Elburg, & Kamenetsky, 2012), the PTV is most similar to MORB suites. This is expected for a mantle upwelling sourced melt due to the reduced nature of the mantle (Li & Aeolus Lee, 2004) , whereas subduction sourced melts have FMQ +1 to +3 (Aeolus Lee et al., 2005). Comparison with average MORB, and Karoo and YSRP suites shows that the V/Sc ratio of the PTV basalts is most similar to the YSRP suite and is thus most likely plume related.

Another factor to consider is the rarity of rhyolites in convergent settings. Their parent magmas erupt first and rhyolites often crystallise quickly as a result of volatile exsolution and are too crystal-rich to erupt (Miller, McDowell, & Mapes, 2003).
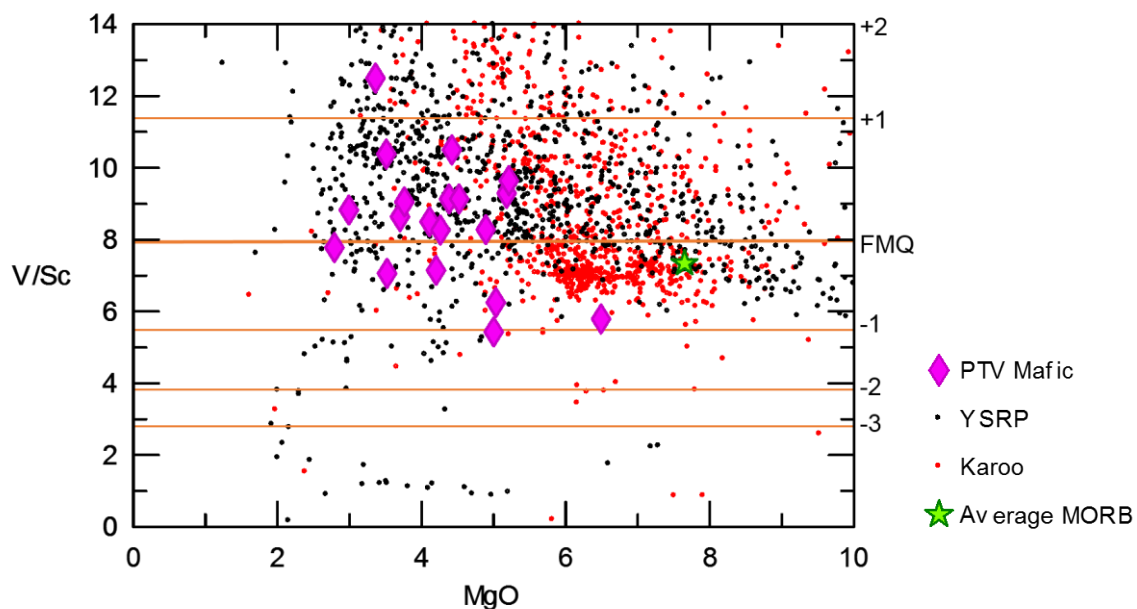
Figure 24: Whole rock V/Sc vs MgO (wt %) in the PTV basalts. horizontal lines represent model fO$_2$-V/Sc contours (right axis) (Aeolus Lee et al, 2005). Basalts from the YSRP (black) and Karoo (red) suites are plotted to show comparisons with contemporary suites. Average MORB (star) also added to show relationship with MORB-like basalts.

The incompatible trace element geochemistry of the PTV basalts compared with NMORB

and OIBs suggest genesis from an OIB-like plume source melt (Figure 25). This is supported

by the PTV being low in the sedimentary stratigraphy, near the onset of rifting (McKenzie,

1978; Needham et al., 1988; White & McKenzie, 1989).
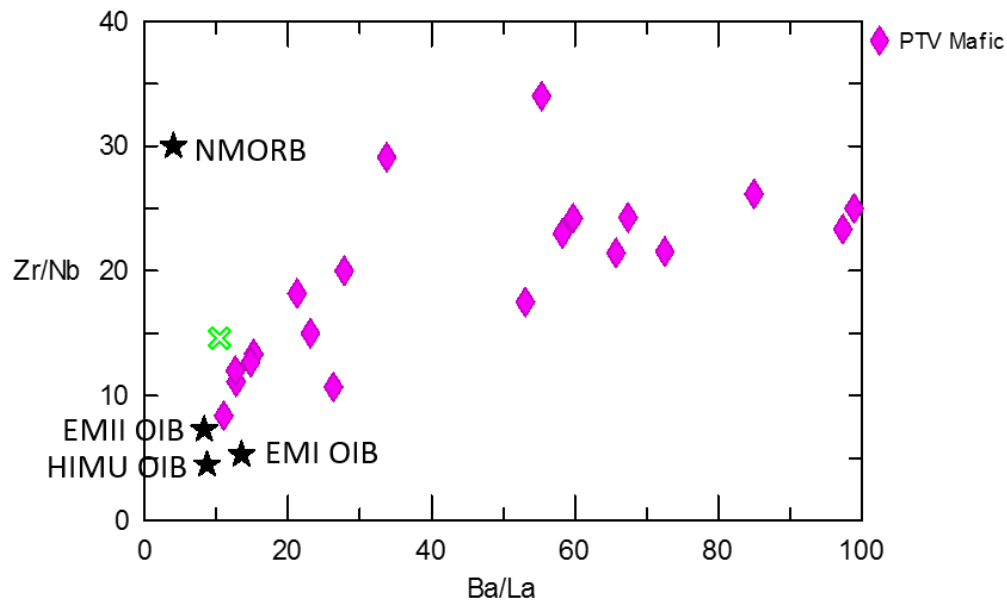
Figure 25: Zr/Nb vs Ba/La diagram showing the trend of the PTV basalts compared to average NMORB and representative OIB end members. The average values are from (Weaver, 1991). A possible PCO crustal contaminant has been marked (green cross).

COMPARISON WITH PAST STUDIES

From these observations, it is reasonable to suggest the PTV formed as a result of the

impingement of a mantle plume and intraplate continental rifting. This is consistent with

Needham's (1985) study on the region that concluded the Edith River Group and the PTV

formed as a result of a NW and ENE rift system with effusive centers on rift faults (Needham

& Stuart-Smith, 1985). Similarly, Needham et al's (1988) study suggested rifting, however

this study used a U-Pb zircon age for the PTV between 1860 and 1870 Ma- too high

compared to the more recently determined age used for this study. The geochemical data

presented here suggests a mantle plume was the cause of rifting, indicating that the PTV was

a direct product of intraplate extension that ultimately lead to the formation of the McArthur

Basin. This suggests that the initiation of the McArthur Basin began due to post plume

extension and subsidence.

CONCLUSIONS

- The Plum Tree Volcanics have potential correlatives in the Davenport Province, McArthur Basin, Mt Isa Inlier and Halls Creek Orogen based on similar stratigraphic, major and trace element features.

- Due to the stratigraphic and geochemical similarities between the PTV and these similarly aged volcanic suites, it is possible that similar tectonic processes occurred across Australia during the Palaeoproterozoic.

- The Plum Tree Volcanics formed as a result of plume impingement and active intraplate continental rifting, as evidenced by ambiguous basalt tectonomagmatic discrimination, crustal features and the bimodality of the suite. The REE pattern of the rhyolites is characteristic of a subduction zone melt, however this can also be representative of a contaminated mantle derived melt.

- An AFC process was the cause of trends in the suite. This is supported by the high $^{87}Sr/^{86}Sr$ ratio in the basalts. The evolved, negative εNd values (approximately -6) shows crustal assimilation occurred during emplacement of the suite. REE trends of this suite show negative Nb and Sr anomalies, and positive Pb anomalies, which are evidence of a crustal contaminant.

- This conclusion is supported by prior studies which focused on tectonics and concluded the region formed as a result of continental rifting. However, due to the age of the PTV used for these studies, they were unable to correctly position the suite at the beginning of rifting.

- Continental rifting, with developing normal faults, rift fault uplift, terrestrial fluvial sediments and conglomerates, and bimodal volcanism record a plume driven melt and continental crustal contamination.

- The provenance of this suite suggests the McArthur Basin began due to post plume extension and subsidence.

REFERENCES

Aeolus Lee, C., Leeman, W. P., Canil, D., & Li, Z. A. (2005). Similar V/Sc Systematics in MORB and Arc Basalts: Implications for the Oxygen Fugacities of their Mantle Source Regions. *Journal of Petrology, 46*(11), 2313-2336. doi: 10.1093/petrology/egi056

Ahmad, M., & Munson, T. J. (2013). Geology and mineral resources of the Northern Territory.

Ahmad, T., Longjam, K. C., Fouzdar, B., Bickle, M. J., & Chapman, H. J. (2009). Petrogenesis and tectonic setting of bimodal volcanism in the Sakoli Mobile Belt, Central Indian shield. *Island Arc, 18*(1), 155-174. doi: 10.1111/j.1440-1738.2008.00651.x

Allen, S. R. (2001). Reconstruction of a major caldera-forming eruption from pyroclastic deposit characteristics: Kos Plateau Tuff, eastern Aegean Sea. *Journal of Volcanology and Geothermal Research, 105*(1-2), 141-162.

Babeyko, A. Y., Sobolev, S. V., Trumbull, R. B., Oncken, O., & Lavier, L. L. (2002). Numerical models of crustal scale convection and partial melting beneath the Altiplano–Puna plateau. *Earth and Planetary Science Letters, 199*(3-4), 373-388.

Bachmann, O., & Bergantz, G. W. (2008). Rhyolites and their Source Mushes across Tectonic Settings. *Journal of Petrology, 49*(12), 2277-2285. doi: 10.1093/petrology/egn068

Bachmann, O., Dungan, M. A., & Bussy, F. (2005). Insights into shallow magmatic processes in large silicic magma bodies: the trace element record in the Fish Canyon magma body, Colorado. *Contributions to Mineralogy and Petrology, 149*(3), 338-349. doi: 10.1007/s00410-005-0653-z

Barberi, F., Santacroce, R., & Varet, J. (1982). Chemical aspects of rift magmatism *Continental and oceanic rifts* (Vol. 8, pp. 223-258): American Geophysical Union Washington, DC.

Betts, P. G., Lister, G. S., & O'Dea, M. G. (1998). Asymmetric extension of the Middle Proterozoic lithosphere, Mount Isa terrane, Queensland, Australia. *Tectonophysics, 296*(3), 293-316. doi: 10.1016/S0040-1951(98)00144-9

Blake, D., & Page, R. (1988). The Proterozoic Davenport province, central Australia: regional geology and geochronology. *Precambrian Research, 40*, 329-340.

Bullen, M. M. (2017). *Isotopic Constraints on the Depositional Environment and Paleo-Redox Conditions of the Greater McArthur Basin, Northern Territory.* (Honours Degree in Geology), The University of Adelaide.

Carr, M. (2002). IGPET for Windows. *Terra Softa Inc., Somerset, NJ*.

Carson, L., Brakel, A., & Haines, P. (1999). Milingimbi, Northern Territory ; 1: 250 000 Geological Map Series, sheet SD53-2. *Northern Territory Geological Survey-Australian Geological Survey Organisation (NGMA), Map and Explanatory Notes*.

Catuneanu, O., Wopfner, H., Eriksson, P., Cairncross, B., Rubidge, B., Smith, R., & Hancox, P. (2005). The Karoo basins of south-central Africa. *Journal of African Earth Sciences, 43*(1-3), 211-253.

Champion, D. C. (2013). *Neodymium depleted mantle model age map of Australia: explanatory notes and user guide*: Geoscience Australia.

Champion, D. C., Budd, A. R., Hazell, M. S., & Sedgmen, A. (2007). *OZCHEM National Whole Rock Geochemistry Dataset*.

Claoué-Long, J., Maidment, D., & Donnellan, N. (2008). Stratigraphic timing constraints in the Davenport Province, central Australia: A basis for Palaeoproterozoic correlations. *Precambrian Research, 166*(1), 204-218. doi: 10.1016/j.precamres.2007.06.021

Cross, A., Claoué-Long, J. C., Scrimgeour, I. R., Ahmad, M., & Kruse, P. D. (2005). Summary of Results: Joint NTGS-GA Geochronology Project: Rum Jungle, Basement to Southern Georgina Basin and Eastern Arunta Region 2001–2003. *Northern Territory Geological Survey Record 2005–2006*.

Daly, R. A. (1925). *The Geology of Ascension Island.* Paper presented at the Proceedings of the American Academy of Arts and Sciences.

DePaolo, D. J. (1981). Trace element and isotopic effects of combined wallrock assimilation and fractional crystallization. *Earth and Planetary Science Letters, 53*, 189-202. doi: 10.1016/0012-821X(81)90153-9

Floyd, P. A., & Winchester, J. A. (1975). Magma type and tectonic setting discrimination using immobile elements. *Earth and Planetary Science Letters, 27*(2), 211-218. doi: 10.1016/0012-821X(75)90031-X

Ghiorso, M. S., & Gualda, G. A. R. (2015). An H2O–CO2 mixed fluid saturation model compatible with rhyolite-MELTS. *Contributions to Mineralogy and Petrology, 169*(6), 53.

Gualda, G. A. R., Ghiorso, M. S., Lemons, R. V., & Carley, T. L. (2012). Rhyolite-MELTS: a modified calibration of MELTS optimized for silica-rich, fluid-bearing magmatic systems. *Journal of Petrology, 53*(5), 875-890.

Hawkesworth, C. J., Norry, M. J., Roddick, J. C., Baker, P. E., Francis, P. W., & Thorpe, R. S. (1979). 143Nd/144Nd,87Sr/86Sr, and incompatible element variations in calc-alkaline andesites and plateau lavas from South America. *Earth and Planetary Science Letters, 42*(1), 45-57. doi: 10.1016/0012-821X(79)90189-4

Hollis, J. A., Carson, C. J., & Glass, L. M. (2009). SHRIMP U–Pb zircon geochronological evidence for Neoarchean basement in western Arnhem Land, northern Australia. *Precambrian Research, 174*(3-4), 364-380. doi: 10.1016/j.precamres.2009.08.010

Jagodzinski, E. (1998). Shrimp U-Pb dating of ignimbrites in the Pul Pul Rhyolite, Northern Territory. *AGSO Res Newsl, 28*, 23-25.

Keen, C. E. (1985). The dynamics of rifting: deformation of the lithosphere by active and passive driving forces. *Geophysical Journal of the Royal Astronomical Society, 80*(1), 95-120. doi: doi:10.1111/j.1365-246X.1985.tb05080.x

Lacasse, C., Sigurdsson, H., Carey, S. N., Jóhannesson, H., Thomas, L. E., & Rogers, N. W. (2006). Bimodal volcanism at the Katla subglacial caldera, Iceland: insight into the geochemistry and petrogenesis of rhyolitic magmas. *Bulletin of Volcanology, 69*(4), 373-399. doi: 10.1007/s00445-006-0082-5

Li, Z. A., & Aeolus Lee, C. (2004). The constancy of upper mantle fO2 through time inferred from V/Sc ratios in basalts. *Earth and Planetary Science Letters, 228*(3-4), 483-493.

Marsh, J. S. (1987). Basalt geochemistry and tectonic discrimination within continental flood basalt provinces. *Journal of Volcanology and Geothermal Research, 32*(1), 35-49. doi: 10.1016/0377-0273(87)90035-7

McAndrew, J., Williams, I., & Compston, W. (1985). A concealed Archaean complex in the Pine Creek Geosyncline, NT *CSIRO Division of Mineralogy and Geochemistry Research Review 1985* (pp. 56-57): CSIRO Melbourne.

McKenzie, D. (1978). Some remarks on the development of sedimentary basins. *Earth and Planetary Science Letters, 40*(1), 25-32.

McKenzie, D., & Bickle, M. J. (1988). The Volume and Composition of Melt Generated by Extension of the Lithosphere. *Journal of Petrology, 29*(3), 625-679. doi: 10.1093/petrology/29.3.625

Meschede, M. (1986). A method of discriminating between different types of mid-ocean ridge basalts and continental tholeiites with the Nb-1bZr-1bY diagram. *Chemical Geology, 56*(3), 207-218. doi: 10.1016/0009-2541(86)90004-5

Miller, C. F., McDowell, S. M., & Mapes, R. W. (2003). Hot and cold granites? Implications of zircon saturation temperatures and preservation of inheritance. *Geology, 31*(6), 529-532.

Needham, R. S., Stuart-Smith, P. G., & Page, R. W. (1988). Tectonic evolution of the Pine Creek Inlier, Northern Territory. *Precambrian Research, 40-41*, 543-564. doi: 10.1016/0301-9268(88)90084-8

Needham, R. S., & Stuart-Smith, P. G. (1985). Stratigraphy and tectonics of the Early to Middle Proterozoic transition, Katherine-El Sherana area, Northern Territory. *Australian Journal of Earth Sciences, 32*(2), 219-230. doi: 10.1080/08120098508729325

Page, R. W. (1996a). *Sample 79125009 (Plum Tree Volcanics)*. Unpublished data in Geoscience Australia's OZCHRON geochronology database: www.ga.gov.au.

Page, R. W. (1996b). *Sample 88126026 (Zamu Dolerite)*. Unpublished data in Geoscience Australia's OZCHRON geochronology database: www.ga.gov.au.

Page, R. W. (1996c). *Sample 83126008 (Grace Creek Granite)*. Unpublished data in Geoscience Australia's OZCHRON geochronology database: www.ga.gov.au.

Page, R. W., & Williams, I. S. (1988). Age of the Barramundi Orogeny in northern Australia by means of ion microprobe and conventional U-Pb zircon studies. *Precambrian Research, 40*, 21-36.

Pankhurst, R. J. R., C. R. (1995). Production of Jurassic rhyolite by anatexis of the lower crust of Patagonia. *Earth and Planetary Science Letters, 134*(1-2), 23-36. doi: 10.1016/0012-821X(95)00103-J

Pearce, J. A. (1996). A user's guide to basalt discrimination diagrams. *Trace element geochemistry of volcanic rocks: applications for massive sulphide exploration. Geological Association of Canada, Short Course Notes, 12*, 79-113.

Pietsch, B. A., Rawlings, D. J., Haines, P. W., & Page, M. (1997). Groote Eylandt region, Northern Territory-1: 250 000 Geological Map Series. *Northern Territory Geological Survey, Explanatory Notes, part of sheets SD53-7, 8*, 11-12.

Rawlings, D. J. (1999). Stratigraphic resolution of a multiphase intracratonic basin system: The McArthur Basin, northern Australia. *Australian Journal of Earth Sciences, 46*(5), 703-723. doi: 10.1046/j.1440-0952.1999.00739.x

Rudnick, R. L., & Gao, S. (2003). Composition of the continental crust. *Treatise on geochemistry, 3*, 659.

Ryerson, F. J., & Watson, E. B. (1987). Rutile saturation in magmas: implications for TiNbTa depletion in island-arc basalts. *Earth and Planetary Science Letters, 86*(2), 225-239. doi: 10.1016/0012-821X(87)90223-8

Scott, D. L., Rawlings, D. J., Page, R. W., Tarlowski, C. Z., Idnurm, M., Jackson, M. J., & Southgate, P. N. (2000). Basement framework and geodynamic evolution of the Palaeoproterozoic superbasins of north-central Australia: an integrated review of geochemical, geochronological and geophysical data. *Australian Journal of Earth Sciences, 47*(3), 341-380. doi: 10.1046/j.1440-0952.2000.00793.x

Sengör, A. M. C., & Burke, K. (1978). Relative timing of rifting and volcanism on Earth and its tectonic implications. *Geophysical Research Letters, 5*(6), 419-421. doi: doi:10.1029/GL005i006p00419

Sigurdsson, H., Houghton, B., McNutt, S., Rymer, H., & Stix, J. (2015). *The Encyclopedia of Volcanoes*: Elsevier.

Stuart-Smith, P. G. (1993). *Geology and mineral deposits of the Cullen mineral field, Northern Territory* (Vol. 229): Australian Government Publishing Service.

Szymanowski, D., Ellis, B. S., Bachmann, O., Guillong, M., & Phillips, W. M. (2015). Bridging basalts and rhyolites in the Yellowstone–Snake River Plain volcanic province: The elusive intermediate step. *Earth and Planetary Science Letters, 415*, 80-89. doi: 10.1016/j.epsl.2015.01.041

Tyler, I. M., Hocking, R. M., & Haines, P. W. (2012). Geological evolution of the Kimberley region of Western Australia. *Episodes, 35*(1), 298-306.

Tyler, I. M., Page, R. W., & Griffin, T. J. (1999). Depositional age and provenance of the Marboo Formation from SHRIMP U–Pb zircon geochronology: implications for the early Palaeoproterozoic tectonic evolution of the Kimberley region, Western Australia. *Precambrian Research, 95*(3-4), 225-243.

Ulmer, P. (2001). Partial melting in the mantle wedge — the role of H2O in the genesis of mantle-derived 'arc-related' magmas. *Physics of the Earth and Planetary Interiors, 127*(1), 215-232. doi: 10.1016/S0031-9201(01)00229-1

Weaver, B. L. (1991). Trace element evidence for the origin of ocean-island basalts. *Geology, 19*(2), 123-126.

White, R., & McKenzie, D. (1989). Magmatism at rift zones: The generation of volcanic continental margins and flood basalts. *Journal of Geophysical Research: Solid Earth, 94*(B6), 7685-7729. doi: 10.1029/JB094iB06p07685

Wilson, M. (1989). Igneous Petrogenesis: Unwin Hyman, London.

Worden, K. E., Carson, C. J., Scrimgeour, I. R., Lally, J., & Doyle, N. (2008). A revised Palaeoproterozoic chronostratigraphy for the Pine Creek Orogen, northern Australia: Evidence from SHRIMP U–Pb zircon geochronology. *Precambrian Research, 166*(1-4), 122-144. doi: 10.1016/j.precamres.2007.05.009

APPENDIX A: FIELD LOCALITIES
Table 3: Table of GPS coordinates for each sample collected

Sample	Latitude	Longitude
PT17-001	14°10'56.64"S	132°11'11.98"E
PT17-002	14°10'56.86"S	132°11'11.35"E
PT17-003	14°10'56.92"S	132°11'10.37"E
PT17-004	14°10'56.73"S	132°11'9.59"E
PT17-005	14°10'56.73"S	132°11'2.68"E
PT17-006	14°10'56.68"S	132°11'1.70"E
PT17-007	14°10'56.67"S	132°11'1.51"E
PT17-008	14°10'56.76"S	132°10'59.37"E
PT17-009	14°10'55.55"S	132°10'55.20"E
PT17-010	14°10'55.92"S	132°10'53.45"E
PT17-011	14°10'52.54"S	132°10'51.07"E
PT17-012	14°10'53.01"S	132°10'49.36"E
PT17-013	14°10'52.73"S	132°10'47.38"E
PT17-014	14°10'52.91"S	132°10'45.53"E
PT17-015	14°10'54.84"S	132°10'42.93"E
PT17-016	14°10'54.85"S	132°10'39.87"E
PT17-017	14°10'55.10"S	132°10'36.57"E
PT17-018	14°10'55.38"S	132°10'36.13"E
PT17-019	14°10'58.09"S	132°10'31.93"E
PT17-020	14°10'59.18"S	132°10'30.81"E
PT17-021	14°10'59.18"S	132°10'30.81"E
PT17-022	14°10'23.40"S	132°10'36.69"E
PT17-023	14°10'24.16"S	132°10'34.17"E
PT18-001, PT18-002, PT18-003	14° 11' 10.68"S	132° 12' 52.58"E
PT18-004	14° 10' 19.29"S	132° 10' 56.19"E
PT18-005	14° 10' 19.04"S	132° 10' 55.57"E
PT18-006	14° 22' 3.70"S	132° 25' 12.62"E
PT18-007	13° 31' 3.28"S	132° 21' 54.22"E
PT18-008	13° 31' 2.78"S	132° 21' 55.06"E
PT18-009	13° 31' 2.97"S	132° 21' 57.03"E
PT18-010	13° 31' 4.62"S	132° 21' 57.54"E
PT18-011	13° 31' 4.39"S	132° 21' 57.64"E
PT18-012	13° 30' 42.01"S	132° 22' 18.98"E
PT18-013	13° 31' 3.83"S	132° 21' 47.90"E
PT18-014	13° 31' 5.12"S	132° 21' 47.34"E
PT18-015	13° 31' 5.22"S	132° 21' 46.96"E
PT18-016	14° 10' 57.16"S	132° 11' 5.90"E
PT18-017	14° 10' 57.21"S	132° 11' 4.33"E
PT18-018	14° 10' 56.27"S	132° 11' 1.15"E
PT18-019	14° 10' 55.02"S	132° 10' 54.92"E

PT18-020	13° 0' 33.00"S	130° 59' 39.15"E
Sample	Latitude	Longitude
E1-1, E1-2	14° 2' 54.88"S	132° 47' 28.28"E
E6-1, E6-2	14° 3' 33.04"S	132° 46' 19.88"E
E9-1, E9-2	14° 4' 37.84"S	132° 44' 53.48"E
D7	13° 46' 40.66"S	132° 39' 22.19"E

APPENDIX B: DRILLCORE SAMPLES

Well name	Interval	Sample taken	Lithology	Sample ID
81 EVDH 1	94.07-94.52m	1/4 core	basalt	E1-2
	206.59-207.05m	1/4 core	basalt	E1-1
81 EVDH 9	106.09-106.66m	1/4 core	rhyolite	E9-2
	120.62-121.15m	1/4 core	rhyolite	E9-1
81 EVDH 6	204.44-204.95m	1/4 core	basalt	E6-2
	205.19-205.63m	1/4 core	basalt	E6-1
829 D7	65.7-70m	chips	rhyolite	D7

Table 4: Reference data for the core intervals sampled from the NTGS core library, Darwin

APPENDIX C: WHOLE ROCK GEOCHEMICAL DATA

Table 5: Whole rock major, minor, and trace element geochemistry for each sample

Sample	PT18-014	PT18-013	PT18-011	PT18-009	PT17-021	PT18-017	PT17-008	PT18-016	PT17-020	PT18-018
Rock Type	Basalt	Basalt	Basalt	Basalt	Basalt	Basalt	Basalt	Basalt	Basalt	Basalt
SiO2	47.54	48.43	48.73	48.79	50.66	50.69	50.94	51.41	51.97	52.11
TiO2	2.42	2.19	2.17	2.18	1.23	0.79	0.82	0.77	1.23	0.8
Al2O3	13.2	13.9	13.9	14.1	14.2	14.7	15.9	14.9	14.4	15.8
Fe2O3	19.40945786	17.05769839	16.95350652	16.70046911	12.89002339	9.243307768	8.871193929	8.707463839	12.57744777	9.5856525
MnO	0.23	0.24	0.23	0.22	0.18	0.12	0.15	0.12	0.17	0.16
MgO	4.2	5.21	5.18	4.89	5.03	4.11	3.7	4.26	5	4.42
CaO	6.82	8.28	8.3	8.38	8.27	7.4	7.25	6.76	7.6	7.78
Na2O	1.81	2.3	2.29	2.57	1.85	2.18	3.09	2.87	1.73	2.28
K2O	1.84	1.57	1.68	1.58	1.59	3.35	2.38	2.26	1.98	3.23
P2O5	0.9578888	0.6324816	0.618732	0.6485228	0.2818668	0.412488	0.3070744	0.3826972	0.2727004	0.3574896
S	0.118	0.091	0.089	0.092	0.081	0.002	<0.001	0.002	0.094	0.002
LOI	1.16	0.29	0.18	0.22	3.75	6.57	6.55	7.06	3.22	2.91
Total	99.70534666	100.19118	100.3212385	100.3709919	100.0128902	99.56779577	99.95826833	99.50216104	100.2441482	99.4351421
Mg#	0.02	0.03	0.03	0.03	0.03	0.03	0.03	0.03	0.03	0.03
Sr	380	500	310	690	610	650	40	400	460	30
Zr	170	140	160	150	150	170	100	230	230	120
Ba	1240	1630	770	2340	2820	2090	748	2470	2450	502
V	200	190	190	210	190	210	220	140	150	170
Be	1	2.5	1	2.5	1.5	2.5	3	2.5	2.5	3
Cl	0.007	0.011	0.012	0.011	0.012	0.012	0.011	0.009	0.008	0.007
Co	47	36	47	39	37	53	34	34	29	43
Cr	80	80	80	70	50	70	120	<10	<10	100
Cs	10.7	1.8	8.7	2.3	1.2	2	1.6	2.3	1.8	1.8
Cu	10	7	10	27	7	8	4	6	1	35
Ga	20	19	20	19.6	17.6	18.6	20	21.4	20	18.2
Hf	3.4	3.6	3.6	3.8	3.4	3.6	3.8	5	4.8	3.6
Li	<10		30	10	20	20	20	90	30	30	90
Nb	5	8	5.5	7	6	7	5.5	10	9.5	5
Ni	8	6	4	16	<2		14	6	4	<2	16
Pb	10	16	11	26	18	23	9	24	20	7
Rb	53.8	112	63.2	115	122	112	68.4	134	111	84
Sb	<0.1	<0.1	0.3	<0.1	<0.1	<0.1	0.8	<0.1	<0.1	1.1
Sc	32	22	35	23	21	23	38	18	17	38
Sn	0.8	0.9	0.9	0.8	0.9	0.9	0.9	1	0.9	0.8
Ta	<0.01	<0.02	<0.03	<0.04	<0.05	<0.06	<0.07	<0.08	<0.09	<0.10
Th	6.1	11.1	6.2	11.1	9.8	10.1	6.8	18.5	17.6	6.2
Tl	0.6	0.3	0.5	0.3	0.2	0.3	0.3	0.5	0.4	0.2
U	1.2	2.4	1.3	2.6	2	2.3	2.5	3.1	3	2
W	72	53	65	78.5	72.5	175	15	65	70.5	22.5
Y	26.6	21.4	26.9	21.4	19.3	20.4	40.2	22	21.4	31.3
Zn	104	78	100	92	84	80	80	108	86	36
La	22.4	30.7	22.8	35.6	28.5	31	35.2	42.4	41	31.4
Ce	48.6	62.7	49.8	68.5	57.8	62.3	51.7	84.9	83.4	48.7
Pr	6.2	7.85	6.35	8.35	7.2	7.65	8.85	10.3	10.1	7.8
Nd	25.3	30.9	25.6	32.4	28.3	29.9	36.3	39	38.5	31.6
Sm	5.2	5.9	5.25	6.15	5.45	5.7	6.9	7.05	7.05	5.95
Eu	1.25	1.25	1.25	1.35	1.15	1.25	1.2	1.4	1.25	1
Gd	5.2	5	5	5	4.6	4.8	7	5.6	5.2	5.8
Tb	0.8	0.7	0.8	0.72	0.64	0.68	0.98	0.76	0.74	0.86
Dy	4.9	3.95	4.9	4	3.6	3.8	5.9	4.2	4.15	5.4
Ho	1.04	0.82	1.04	0.86	0.74	0.78	1.26	0.86	0.86	1.22
Er	3.1	2.35	3.15	2.4	2.1	2.25	3.6	2.5	2.4	3.6
Tm	0.4	0.35	0.4	0.35	0.3	0.3	0.45	0.35	0.35	0.45
Yb	2.85	2.15	2.85	2.15	2	2.05	3.1	2.3	2.3	3.25
Lu	0.46	0.32	0.44	0.32	0.42	0.3	0.44	0.46	0.4	0.46

Tectonic Provenance of the Plum Tree Volcanics

Sample	PT17-007	PT17-005	PT17-006	PT17-018	E1-1	PT17-004	E1-2	PT17-001	PT17-019	E6-1
Rock Type	Basalt	Basalt	Basalt	Basalt	Basalt	Basalt	Basalt	Basalt	Rhyolite	Basalt
SiO2	52.12	52.33	52.73	55.14	55.26	55.54	55.57	56.51	57.23	58.64
TiO2	0.81	0.78	0.81	1.35	1.2	0.93	1.21	0.92	1.34	0.64
Al2O3	15.8	15.7	15.8	15.3	13.9	16.7	13.7	16.5	15.6	18.1
Fe2O3	9.511229732	9.853574464	9.779151696	10.85083955	13.06863804	10.91037777	12.94956161	9.079577679	11.13364607	8.201389018
MnO	0.18	0.16	0.16	0.11	0.21	0.1	0.16	0.09	0.09	0.05
MgO	4.52	3.76	4.38	6.49	3.51	2.79	3.36	2.99	4.91	3.52
CaO	7.59	6.47	7.77	0.52	5.09	2.57	5.02	3.7	0.41	0.66
Na2O	2.09	2.36	2.11	0.06	2.66	2.8	3.17	2.97	0.04	0.94
K2O	3.2	3.91	3.28	4.34	2.43	3.98	2.61	3.76	4.68	5.19
P2O5	0.3460316	0.3254072	0.3391568	0.3024912	0.1879112	0.355198	0.1924944	0.366656	0.2887416	0.1352044
S	<0.001	<0.001	0.002	<0.001	0.035	<0.001	0.027	<0.001	0.003	0.004
LOI	3.21	4.44	2.71	5.05	2.52	3.54	2.15	3.24	4.38	4.04
Total	99.37726133	100.0889817	99.8703085	99.51333075	100.0715492	100.2155758	100.119056	100.1262337	100.1053877	100.1205934
Mg#	0.04	0.03	0.03	0.02	0.03	0.02	0.02	0.02	0.02	0.01
Sr	300	260	190	290	200	360	280	80	230	150
Zr	230	210	250	230	240	330	330	290	270	330
Ba	1820	2780	2560	2370	2780	3610	4550	1870	1870	3680
V	70	70	30	30	20	20	10	9	10	9
Be	2.5	2.5	3	3	3	3	3	3.5	3.5	2.5
Cl	0.009	0.009	0.006	0.006	0.009	0.006	0.007	0.008	0.005	0.009
Co	23	32	19	27	18	37	33	23	36	26
Cr	50	50	<10	20	<10	<10	<10	<10	<10	<10
Cs	2.8	2.8	3.9	1.8	3	2.7	3.2	2.4	1.6	2.4
Cu	2	4	10	6	5	5	6	6	6	6
Ga	20.4	19	21.6	20.2	20.6	21	20	20.4	20.4	18.8
Hf	5.6	5.2	6.8	4	6.4	6.8	7.2	5.6	7.4	5
Li	10	20	20	<10	10	10	20	10	10	<10
Nb	11.5	11	13	8.5	11	12	11	8	10	8.5
Ni	<2	6	<2	<2	4	<2	<2	<2	<2	<2
Pb	18	22	13	14	13	18	38	10	17	24
Rb	126	118	189	124	170	199	186	156	154	164
Sb	0.2	0.5	0.2	<0.1	0.3	0.3	0.2	0.3	0.2	0.2
Sc	14	14	11	11	9	11	10	10	8	9
Sn	2.6	2.2	1.8	1.4	2.3	2.1	2.1	1.8	2.1	2.2
Ta	<0.11	<0.12	<0.13	<0.15	<0.16	<0.17	<0.18	<0.19	<0.20	<0.21
Th	21.9	21	23.1	23.2	24.6	22.4	24.9	29.6	33.9	29.8
Tl	0.8	0.8	0.7	0.5	0.8	0.7	0.8	1	0.7	1
U	4.7	4.4	4.5	4.7	5	4.7	5.1	5.9	6.6	5.6
W	70.5	126	91	119	69.5	164	165	66	186	89
Y	27.4	25.8	22.6	23.5	25.9	25.1	23.1	26.2	32.6	24.7
Zn	66	74	70	62	58	96	54	46	54	54
La	47.3	44.4	50.3	55.5	57.8	56.8	64	62.7	65.9	61.1
Ce	94.2	87.8	97.2	107	113	107	120	122	130	116
Pr	11.4	10.5	11.6	12.7	13.1	12.6	13.9	14.1	14.9	13.6
Nd	42.5	39.6	42.6	45.7	46.4	45.1	50.1	49.2	53.1	48.3
Sm	7.7	7.25	7.65	7.75	7.85	7.7	8.2	8.5	8.95	8.35
Eu	1.2	1.15	1.55	1.5	1.55	1.6	1.75	1.25	1.1	1.4
Gd	6	5.8	5.8	5.8	6	5.8	5.8	6.2	6.8	6
Tb	0.86	0.82	0.8	0.82	0.84	0.8	0.82	0.92	0.98	0.84
Dy	5.05	4.8	4.3	4.45	4.75	4.45	4.4	5	5.75	4.6
Ho	1.04	1	0.88	0.9	0.98	0.9	0.9	1.04	1.2	0.94
Er	3.05	2.8	2.55	2.6	2.8	2.6	2.55	2.95	3.45	2.7
Tm	0.4	0.4	0.35	0.35	0.4	0.35	0.35	0.4	0.45	0.35
Yb	2.85	2.65	2.4	2.4	2.6	2.4	2.45	2.85	3.1	2.6
Lu	0.42	0.44	0.38	0.34	0.38	0.44	0.42	0.46	0.48	0.34

Sample	PT17-002	PT17-003	PT17-011	PT17-009	PT17-014	PT17-010	PT18-004	PT17-012	PT18-008	PT18-010
Rock Type	Rhyolite	Rhyolite	Rhyolite	Rhyolite	Rhyolite	Rhyolite	Rhyolite	Rhyolite	Rhyolite	Rhyolite
SiO2	61.3	61.8	63.36	63.78	64.24	64.26	65	65.27	65.32	66.44
TiO2	0.63	0.63	0.58	0.56	0.4	0.54	0.4	0.43	0.55	0.71
Al2O3	14.9	14.5	16	15.5	15.2	16.3	15.5	14.9	15	16.8
Fe2O3	6.147320625	6.593857232	5.284016518	5.239362857	4.003944911	4.986325446	4.033714018	4.777941696	6.742702768	4.271866875
MnO	0.1	0.09	0.07	0.1	0.07	0.11	0.08	0.05	0.03	0.04
MgO	1.49	2.11	1.03	1.09	0.59	1.02	0.75	0.71	1.25	1.21
CaO	3.43	2.42	2.58	2	2.98	1.27	2.19	2.37	0.38	0.35
Na2O	2.43	2.6	2.65	4.23	2.8	3.65	2.73	2.6	3.44	1.7
K2O	4.4	5.27	4.74	4.29	4.85	5.61	5.47	5.49	6.02	6.13
P2O5	0.2337432	0.2429096	0.1879112	0.1764532	0.1054136	0.1672868	0.11458	0.1191632	0.1558288	0.1993692
S	<0.001	<0.001	0.002	0.002	<0.001	0.003	0.003	0.004	<0.001	0.003
LOI	4.54	3.38	3.49	2.24	3.7	1.81	3.15	2.86	1.1	1.96
Total	99.60106383	99.63676683	99.97392772	99.20781606	98.93935851	99.72661225	99.42129402	99.5811049	99.98853157	99.81423608
Mg#	0.03	0.03	0.03	0.04	0.03	0.04	0.04	0.02	0.01	0.02
Sr	110	70	70	1870	920	460	260	100	70	200
Zr	150	200	260	620	410	270	290	250	290	380
Ba	1290	606	620	120	50	40	3010	2560	240	1410
V	9	70	70	30	20	10	1	1	30	30
Be	3	2.5	2.5	1.5	1	1	3	3	3	3.5
Cl	0.008	0.005	0.003	0.005	0.004	0.008	0.004	0.009	0.006	0.042
Co	35	34	37	19	20	37	17	19	15	32
Cr	<10		50	50	70	50	140	<10	<10	<10	<10
Cs	1.6	5.3	4.7	0.6	0.3	1.5	3.6	2.6	3.1	1.2
Cu	2	28	7	10	4	3	3	3	9	<1
Ga	18.8	17.4	14.2	16.6	16.4	12	21.8	21.6	23.8	25.2
Hf	4.6	3.2	6.2	12.4	9.2	7.4	7	7	6.2	8.2
Li	<10		20	<10		30	30	20	10	20	<10	20
Nb	9.5	9	8	9.5	7	14.5	13	13	13.5	15
Ni	<2		32	<2		8	8	10	<2	6	6	8
Pb	10	9	14	19	10	9	14	7	6	16
Rb	170	166	128	19.4	25.6	29	211	211	212	189
Sb	0.7	0.9	1.5	1.6	0.8	1.9	0.3	0.4	1	0.3
Sc	7	12	11	9	8	9	9	8	8	10
Sn	3	2.5	2.1	8.7	5.5	21.8	2.4	2.5	3.7	3.4
Ta	<0.22	<0.23	<0.24		1	0.7	1.5	0.7	0.6	0.7	0.8
Th	37.1	17.3	14.6	54.8	43.9	42.5	24.4	26.1	29.5	28.3
Tl	1	0.7	0.6	<0.1	<0.1	<0.1		1	1	0.6	1
U	5.5	3.9	2.8	3.2	2.5	1.7	4.7	5.2	3.8	6.1
W	147	120	125	107	102	223	91.5	95	72.5	184
Y	43.6	28.7	23	33.2	25	22.9	23.9	24.7	34	43.2
Zn	36	96	22	10	6	14	72	52	36	26
La	107	50.5	47.8	149	79.2	33.7	59.8	61.3	80.4	74.1
Ce	135	102	91.8	419	157	90.9	111	113	160	140
Pr	21.4	12.3	10.8	37.6	18	8.6	13	13.2	20.4	17.2
Nd	75.3	45.7	38.4	125	62.4	30.2	45.6	45.9	71.4	61.4
Sm	12	8.75	6.8	22.4	11.6	5.85	8.1	7.95	12.5	11.3
Eu	1.1	1.2	0.95	4.5	2.35	1.05	1.85	1.65	1.65	1.65
Gd	9.4	6.8	5.2	17.6	9.6	5	6.2	6.4	9.2	9.6
Tb	1.28	0.92	0.7	2	1.16	0.72	0.82	0.84	1.22	1.32
Dy	6.8	5.1	4	8.65	5.65	4.4	4.65	4.75	6.65	7.75
Ho	1.42	1.1	0.8	1.36	1.06	0.92	0.88	0.92	1.2	1.52
Er	4	3.2	2.4	4.25	3.65	3.4	2.65	2.8	3.55	4.55
Tm	0.5	0.45	0.35	0.7	0.6	0.6	0.35	0.4	0.5	0.65
Yb	3.45	3.15	2.15	5	4.4	4.35	2.5	2.65	3.15	4.25
Lu	0.52	0.48	0.32	0.76	0.62	0.64	0.36	0.4	0.54	0.68

Tectonic Provenance of the Plum Tree Volcanics

Sample	PT18-019	PT18-015	PT18-005	PT18-012	D7	PT17-016	E9-2	PT18-007	PT17-013	E6-2
Rock Type	Rhyolite	Rhyolite	Rhyolite	Rhyolite	Rhyolite	Rhyolite	Rhyolite	Rhyolite	Rhyolite	Rhyolite
SiO2	66.65	66.7	66.9	66.93	67.8	67.81	68.02	68.19	68.81	69.23
TiO2	0.43	0.62	0.34	0.57	0.66	0.34	0.57	0.57	0.34	0.53
Al2O3	15	14.3	14.8	14.3	17.3	14.9	14.1	14.1	14.8	13.3
Fe2O3	4.167675	6.474780804	3.765792054	5.730553125	3.631831071	3.274601786	5.507284821	5.105401875	3.408562768	4.435596964
MnO	0.07	0.05	0.07	0.06	<0.01	0.06	0.07	0.04	0.04	0.04
MgO	0.79	1.25	1.32	1.04	1.67	1.16	1.15	0.76	0.52	1.91
CaO	1.77	0.97	1.41	0.27	0.11	1.2	0.54	0.51	1.23	1.82
Na2O	3.46	2.57	2.15	0.91	0.03	2.42	3.02	2.03	3.96	1.84
K2O	5.14	4.84	5.64	8.64	5.35	5.73	5.69	7.18	4.93	3.24
P2O5	0.1237464	0.17187	0.091664	0.1695784	0.0504152	0.0824976	0.1627036	0.160412	0.0939556	0.1329128
S	0.002	<0.001	0.002	0.004	0.017	0.002	0.013	<0.001	0.002	0.01
LOI	2.06	1.76	3.26	1.3	3.4	2.84	1.29	1.18	1.65	3.46
Total	99.6634214	99.7066508	99.74945605	99.92413153	100.0192463	99.81909939	100.1329884	99.82581388	99.78451837	99.94850976
Mg#	0.03	0.02	0.04	0.02	0.01	0.04	0.02	0.02	0.02	0.02
Sr	140	340	160	360	130	360	270	130	780	800
Zr	340	250	450	280	330	270	310	300	140	140
Ba	1040	440	1630	470	2770	420	980	1100	2580	2430
V	40	240	40	260	30	270	200	20	190	170
Be	2.5	1.5	4	1.5	2.5	1.5	2	3.5	1.5	2
Cl	0.025	0.029	0.033	0.166	0.022	0.117	0.303	0.019	0.006	0.006
Co	35	64	18	59	25	67	53	27	33	36
Cr	<10	30	<10	30	<10	30	30	<10	70	70
Cs	0.6	1.2	1.7	1.7	1	2.3	3.5	1.3	0.8	2
Cu	<1	37	3	43	<1	42	59	4	15	12
Ga	25.2	26	33.6	24	24	26.2	26.2	26.2	18.2	20
Hf	8	5.4	9.8	5	7.8	5.4	6.4	8	2.8	3.6
Li	30	20	50	20	20	20	50	50	30	20
Nb	14	22.5	19	21	15.5	22.5	29	15	6	6.5
Ni	10	34	8	34	8	32	24	8	14	14
Pb	7	8	18	13	12	10	1150	17	19	22
Rb	199	45	195	49	235	50.8	83.2	174	63.4	94.4
Sb	0.3	<0.1	0.3	<0.1	0.3	<0.1	0.9	0.4	<0.1	<0.1
Sc	10	29	13	28	9	28	28	10	23	20
Sn	4.6	1.4	3.8	1.4	3.5	1.4	3.8	3.5	0.9	1
Ta	0.6	1.3	1.1	1.1	0.8	1.4	2	0.8	0.4	<0.1
Th	28.1	5.3	34.8	5.2	27.4	5.1	6	28.9	8	9.8
Tl	0.7	0.3	0.8	0.3	0.9	0.3	0.4	0.7	0.3	0.2
U	6.5	0.9	7.6	0.9	6.1	0.9	1.1	6.6	1.7	1.9
W	170	90	91.5	67	116	66	52.5	134	46	48.5
Y	38.4	36.8	60.5	34.9	41.2	36.9	44.5	42.8	17.4	20.7
Zn	30	142	36	166	24	156	2210	52	82	76
La	81.1	34.5	75.1	30.9	72.2	33.2	37.2	69.5	26.5	33.5
Ce	150	71.2	146	66.9	135	69	79.8	136	55	63.4
Pr	18.3	9.95	18.1	9	16.3	9.65	11.3	16.4	7	7.95
Nd	64.4	41	65.7	37.4	58.5	40.8	48.4	59.2	27.3	30.9
Sm	11.4	9	12.2	8.3	10.7	9	10.8	11.1	4.7	6.2
Eu	1.7	2.7	1.55	2.5	1.6	2.65	2.85	1.65	1.75	1.7
Gd	9.2	9	10.8	8.4	9	9	11.2	9.8	5	5.4
Tb	1.24	1.26	1.58	1.16	1.28	1.26	1.58	1.36	0.7	0.72
Dy	7.05	7.2	9.8	6.65	7.5	7.25	9.1	7.85	3.85	4.1
Ho	1.38	1.4	2.04	1.28	1.48	1.4	1.7	1.54	0.72	0.78
Er	4.15	3.95	6.35	3.7	4.4	4	4.85	4.55	2.05	2.3
Tm	0.6	0.55	0.9	0.5	0.65	0.55	0.75	0.65	0.3	0.3
Yb	4.1	3.45	5.6	3.15	4.1	3.35	4.2	4.3	1.95	2.1
Lu	0.64	0.56	0.88	0.44	0.64	0.56	0.62	0.66	0.3	0.32

Tectonic Provenance of the Plum Tree Volcanics

Sample	PT17-015	PT18-001	PT18-003	E9-1	PT17-017	PT18-006	PT17-022	PT18-002	PT18-020	PT17-023
Rock Type	Rhyolite	Rhyolite	Rhyolite	Rhyolite	Rhyolite	Rhyolite	Rhyolite	Rhyolite	Rhyolite	Rhyolite
SiO2	69.59	70.39	71.31	72.28	72.71	72.77	72.9	75.08	76.73	78.22
TiO2	0.36	0.59	0.25	0.36	0.24	0.45	0.65	0.57	0.11	0.65
Al2O3	14.6	15.3	10.6	12.7	13.8	14.5	12.3	15.3	12.7	10.8
Fe2O3	3.185294464	6.891548304	13.9765958	3.423447321	3.051333482	4.405827857	6.087782411	2.619681429	1.190764286	4.5844425
MnO	0.03	<0.01	0.01	0.04	0.03	<0.01	0.01	0.01	<0.01	0.01
MgO	0.43	0.05	0.06	0.8	0.72	0.66	0.94	0.04	0.96	0.32
CaO	0.93	0.08	<0.01	0.74	0.39	0.04	0.15	0.03	<0.01	0.02
Na2O	2.65	0.02	0.01	2.33	2.13	0.04	0.1	<0.01	0.39	0.33
K2O	6.04	0.87	0.72	5.48	4.73	4.73	3.39	1.23	6.32	2.73
P2O5	0.1099968	0.63019	0.1512456	0.0847892	0.0618732	0.0504152	0.206244	0.2360348	0.0206244	0.0641648
S	0.007	0.049	0.012	0.01	0.006	<0.001	0.006	0.024	<0.001	<0.001
LOI	1.69	4.99	3.3	1.73	1.99	2.27	2.64	4.6	1.54	1.73
Total	99.62229126	99.8607383	100.3998414	99.97823652	99.85920668	99.91624306	99.38002641	99.73971623	99.96138869	99.4586073
Mg#	0.02	0.00	0.00	0.02	0.02	0.00	0.00	0.01	0.02	0.00
Sr	780	300	40	50	220	210	60	100	70	110
Zr	170	210	50	330	150	180	130	140	220	300
Ba	2660	2380	350	130	730	880	600	400	650	1230
V	210	1	1	40	270	300	120	60	30	20
Be	2	3	3	5.5	1.5	1.5	4	3	3	3
Cl	0.011	0.004	0.001	0.008	0.012	0.018	0.003	0.008	0.019	0.018
Co	37	29	27	10	55	48	25	25	35	28
Cr	60	<10	<10	<10	20	<10	70	50	<10	<10
Cs	2.8	2.2	1.9	9.1	1.3	0.8	10.1	7.2	2.4	2.9
Cu	10	2	<1	<1	107	106	48	26	14	10
Ga	19.8	22.2	24	32.4	25	23	33.4	22.2	24.8	26.2
Hf	3.6	6.8	3.8	9.6	4.6	4.4	4.4	5.4	7.8	8
Li	20	10	10	10	30	40	30	20	10	20
Nb	6.5	12	23	19	10	9	15.5	13.5	11	15.5
Ni	16	6	8	8	30	30	54	34	8	14
Pb	24	13	11	5	13	6	7	7	7	11
Rb	107	175	383	164	81.4	83.4	260	171	217	203
Sb	0.7	0.2	<0.1	0.6	0.6	0.3	2	1.5	0.8	1
Sc	20	9	4	12	26	24	17	10	6	11
Sn	0.9	2.5	4.9	4.6	1.7	1.4	5.6	3.8	4.4	3.5
Ta	<0.1	0.4	2.8	1.3	0.7	0.3	1.3	0.8	0.6	0.8
Th	10.3	28.1	42.6	36.9	9.9	9.4	22.2	19.1	44	27.8
Tl	0.3	0.7	1.2	0.3	0.3	0.3	1.2	0.8	1.1	1
U	2.2	5.3	12	7	2.6	2.4	5	4.3	8.8	6
W	65.5	143	165	46	57.5	45	37	107	147	149
Y	20.5	27.3	20.1	46.1	28.7	26.6	33.4	29.3	45.8	42.9
Zn	92	60	10	56	130	82	132	76	44	86
La	31.3	63.5	73.6	52.2	31.6	31.6	54.3	48.6	83.1	72.2
Ce	61	118	102	107	63.6	61.7	105	94.1	157	136
Pr	7.65	14	12.3	13.4	7.95	7.8	12.9	11.6	18.9	16.5
Nd	29.7	49.3	37.6	49.3	30.6	30	46.6	41.5	64.8	59.7
Sm	5.85	8.5	5.15	10.6	6.05	6	8.7	7.7	11.7	11
Eu	1.65	1.75	0.7	1.75	1.55	1.5	1.4	1.45	0.95	1.7
Gd	5.2	7	3.8	9.6	6	5.8	7.2	6.8	9.8	9.6
Tb	0.7	0.94	0.5	1.36	0.9	0.84	1.04	0.9	1.4	1.32
Dy	4.05	5.2	2.8	8.2	5.3	5.15	6.1	5.45	8.3	7.65
Ho	0.78	1.02	0.6	1.64	1.06	1.04	1.14	1.04	1.66	1.52
Er	2.35	3.05	1.95	4.9	3.1	3.15	3.4	3.15	4.9	4.5
Tm	0.3	0.45	0.4	0.7	0.5	0.45	0.55	0.45	0.7	0.65
Yb	2.1	2.8	2.3	4.55	2.95	2.9	3.3	3.05	4.7	4.15
Lu	0.28	0.46	0.4	0.74	0.44	0.46	0.48	0.44	0.68	0.66

APPENDIX D: ISOTOPE GEOCHEMISTRY

Table 6: Summary of Nd, Sm, and Sr isotopes determined by TIMS. Calculated model ages are based on ratios taken from Goldstein et al. (1984).

Sample	Age (Ma)	Sm (ppm)	Nd (ppm)	147Sm/144Nd	143Nd/144Nd	143Nd/144Nd (t)	2σ	εNd	εNd (t)	DM (t)	Rb (ppm)	Sr (ppm)	87Sr/86Sr	2σ	87Sr/86Sr (t)
PT17-001	1825	7.05	38.5	0.1141	0.511258	0.509821	2.82	-28.22	-8.94	2955	111	460	0.726324	4.84	0.7079619
PT17-002	1825	7.7	42.5	0.1111	0.511323	0.509924	5.52	-26.92	-6.93	2773	126	300	0.746923	6.06	0.714898
PT17-006	1825	5.7	29.9	0.115	0.511414	0.50997	3.34	-25.1	-6.02	2740	112	650	0.718566	5.51	0.7054638
PT17-015	1825	8.35	48.3	0.1023	0.511248	0.509961	2.02	-28.26	-6.19	2648	164	150	0.792994	5.34	0.7092528
PT17-017	1825	12	75.3	0.0975	0.511262	0.510025	1.99	-28.13	-4.94	2532	170	110	0.854486	7.41	0.7354097
PT17-021	1825	5.2	25.3	0.1262	0.511547	0.509964	2.35	-22.6	-6.15	2867	53.8	380	0.716844	6.16	0.7060807

APPENDIX E: EXTENDED METHODS

Sample Collection

1. Samples were collected from various localities in the Katherine- Pine Creek region
2. Drill core samples were collected from the NTGS Core Library in Darwin.
3. Core samples were selected using the NTGS' online STRIKE system to identify drill holes near the PTV, and GEMIS was used to search for well reports relating to those drill holes to identify wells that intersected the PTV

Whole Rock Geochemistry

1. A diamond tipped saw was used to remove weathered surfaces from the samples and cut them to an appropriate size. Unused sample was preserved.
2. Samples were crushed into gravel using the University of Adelaide jaw crusher. Half of the gravel was preserved.
3. The gravels were milled into a powder using a tungsten carbide mill head. Half of the powder was preserved.
4. Powders were sent to Bureau Veritas, who undertook the following geochemical analyses:
    a. XRF for major elements
    b. ICP-MS for minor elements
    c. ICP-OES for trace elements

Whole Rock Radiogenic Isotope Geochemistry (Nd-Sm-Sr)

Cleaning Vials

1. Sixteen 7mL and five 15mL vials were washed with acetone
2. Vials were washed with 6M hydrochloric acid (HCl) on a hotplate
3. Vials were rinsed 3 times with deionised (di) water
4. Vials placed in a jar and rinsed 3 times with di water
5. Vials were transferred to a Teflon jar, filled with 6M nitric acid (HNO_3) at 170˚C for 2 days
6. $HNO3_3$ was emptied and the jar was rinsed 3 times with di water
7. The jar was filled with 6M HCl and placed back on the hotplate at 170˚C for 2 days
8. Acid was emptied and the jar was rinsed 3 times with di water
9. The jar was filled with di water and placed back on the hotplate at 170˚C overnight
10. The jar was rinsed 3 times with di water
11. 2mL 15M HNO_3 and 1mL 28M hydrofluoric acid (HF) was added to each vial, each lid was tightened and vials were placed on a hotplate at 140˚C and leave overnight
12. The acids were emptied

Sample Preparation

1. Spikes Sm/Nd G and Sr F were used as a blank in a Teflon 'bomb'
2. Spike Sm/Nd H was added to standard Granite G2 in a Teflon bomb
3. Spike Sm/Nd H was added to a weighed mass of each sample pulp in 15mL vials using a Metler Toledo AT201 electronic balance
4. 2mL 15M HNO_3 and 4mL 28M HF were added to vials, which were secured and placed on a hotplate at 140˚C for 2 days, Teflon bomb lids were secured and heated for 2 hours

5. 2mL 15M HNO_3 was added to the Teflon bombs and evaporated for 1 hour
6. 2mL 15M HNO_3 and 4mL 28M HF was added to bombs
7. Bombs were secured in metal jackets and placed in an oven at 200˚C for 4 days
8. Bombs were evaporated to almost dryness, 2mL 15M HNO_3 was added and left to evaporate for an hour. 6mL 6M HCl was added and bombs were placed back in the oven at 200˚C overnight
9. Vials were evaporated to near dryness on the same hotplate, 2mL 15M HNO_3 was added and left to evaporate for one hour.
10. Vials were filled with 2mL 15M HNO_3 and 4mL 28M HF and left on the hotplate at 140˚C for 2 days
11. Vials were evaporated to near dryness, 2mL 15M HNO_3 was added and left to evaporate for one hour, 6mL 6M HCl was added to each vial. Vials were placed on a hotplate at 140˚C overnight.
12. HCl was evaporated from all bombs and vials
13. 1.5mL 2M HCl was added to bombs and vials and residue was dissolved. Liquid was poured into 2mL centrifuge tubes.
14. Centrifuge tubes were centrifuged by an Eppendorf Centrifuge 5415 D for 5 minutes at 13,200 rpm.

Initial Column Chromatography

1. Columns were loaded with 2mL AG 50W-X8 200-400 mesh cation exchange resin
2. 10mL 6M single distilled (sd) HCl was added to each column and allowed to drip through
3. 5mL di water was added to each column and allowed to drip through
4. 10mL 6M sd HCl was added to each column and allowed to drip through
5. 5mL di water was added to each column and allowed to drip through
6. The tip of the column was rinsed with 6M sd HCl
7. 6mL 2M sd HCl was added to each column and allowed to drip through
8. Each sample was loaded with 1mL 2M sd HCl
9. 1mL 2M sd HCl was used to wash each column. This was done twice
10. 8mL 2M sd HCl was discarded through each column
11. 2mL 3M sd HCl was discarded through each column
12. 2mL 3M sd HCl was collected in a 7mL vial, this contained Sr
13. Sr vials were evaporated on a hotplate at 140˚C
14. 1mL 6M sd HCl was discarded through each column
15. 5mL 6M sd HCl was collected in a 7mL vial, this contained Nd and Sm
16. Nd/Sm vials were evaporated on a hotplate at 140˚C
17. 10mL 6M sd HCl was used to clean each column
18. 5mL di water was added to each column and allowed to drip through
19. 10mL 6M sd HCl was added to each column and allowed to drip through
20. 5mL di water was added to each column and allowed to drip through
21. The columns were recapped and returned with new acid to their rack

Sr Columns

1. Columns were removed from their storage container and rinsed 3 times with DI water
2. Columns were loaded with 200uL Eichrom Sr resin SPS (part# SR-B50-S, 50-100u, 50g) using a 1mL pipette
3. The resin and columns were washed with 1mL 8M sd HNO_3 3 times
4. The resin and columns were washed with 1mL DI water 3 times
5. The resin and columns were washed with 1mL 8M sd HNO_3 3 times

6. The resin and columns were washed with 1mL DI water 3 times
7. The resin was equilibrated by adding 1mL 8M HNO_3 3 times
8. The Sr sample was loaded in 1mL 8M sd HNO_3
9. The sample was washed 5 times with 1mL 8M HNO_3
10. Sr was collected with 1mL 0.05M sd HNO_3 6 times
11. 1 drop of 0.1M phosphoric acid (H_3PO_4) to each Sr vial
12. Vials were dried on a hotplate at 140˚C
13. Approximately 0.5mL of 15M HNO_3 was added to oxidise any organics
14. Vials were dried on a hotplate at 140˚C overnight
15. Resin was emptied from columns into waste and columns were recycled

Sm/Nd Columns

1. Columns were removed from their storage rack and allowed to drain. Columns used 1mL Eichrom Ln resin SPS (part# LNS05152)
2. The tip of the columns was rinsed with 0.16M HCl
3. 4mL 0.16M HCl was used to equilibrate each column
4. The samples were loaded with 0.5mL 0.16M HCl
5. 1mL 0.16M HCl was added to each column
6. 1mL 0.16M HCl was added to each column
7. 13mL 0.16M HCl was added to each column
8. 0.5mL 0.27M HCl was added to each column
9. 3.5mL 0.27M HCl was added to the columns and collected in a new 7mL vial, this contained Nd
10. 2mL 0.27M HCl was added to each column
11. Sm/Nd vials were cleaned by heating with 6M HCl
12. 3mL 0.5M HCl was added to each column and collected in original Sm/Nd vials, this contained Sm
13. 1 drop of 0.1M H_3PO_4 was added to each sample
14. Vials were evaporated overnight. 15M HNO_3 was added after complete dryness to dissolve organics
15. 10mL 6M sd HCl was added to each column
16. 10mL 6M HCl was added to each column
17. 2mL 0.5M HCl was added, column stems were rinsed and the columns were replaced in their tubes with 0.5M HCl

Mass Spectrometer Filament Preparation

1. 10 inner, 10 outer, and 20 centre mass spectrometer filament holders were prepared by cutting off the used rhenium filaments and grinding off the remains with a hand grinder
2. Filament holders were placed in a large beaker and washed in 30% hydrogen peroxide (H_2O_2) on a hotplate at 80˚C for one hour
3. Filament holders were rinsed 3 times with di water
4. Holders were placed in a container with acetone in an ultrasonic bath for one minute
5. Holders were put in an oven at 100˚C for 3 hours
6. Rhenium ribbon was welded onto the filaments
7. Filaments were loaded into an Isotopx DG60 degasser. A vacuum was created overnight, and filaments were degassed the following day

Thermal Ionisation Mass Spectrometry (TIMS)

1. Centre Re filaments were loaded into an Isotopx Filament Loading Unit

2. 1uL 1M H_3PO_4 was loaded onto each filament and evaporated at 0.5A (current was controlled by a G^w Instek PSP-405)
3. 0.5uL Birck's Solution (2g $TaCl_5$, 1.2mL 50% HF, 1.2mL 85% H_3PO_4, 20mL 70% HNO_3, 80mL H_2O) was added to each filament and evaporated
4. Approximately 500ng Sr was loaded in 1uL Bircks Solution and dried at 0.5A
5. Current was increased to 1A
6. Current was increased to 1.8A and left for 1 minute
7. Current was gradually increased until filaments were just turning red for several seconds, then turned down to 0A
8. Outer Re filaments were loaded into Isotopx Filament Loading Unit
9. 0.5uL H_3PO_4 was loaded onto each filament and dried at 0.5A
10. Half of the Nd sample was loaded into 1uL Sm/Nd loading solution (1M HNO_3 + 1% H_3PO_4) and added to each filament
11. Current was increased to 1A
12. After samples were dry, current was increased to 1.8A and left for 1 minute
13. Current was increased until filaments were slightly red for a few seconds and turned down to 0A.
14. After Nd analysis, Sm was loaded onto the same outer filament and prepared using the same method as Nd
15. Samples were analysed in an Isotopx Phoenix mass spectrometer

Analytical Methods

IgPet

1. 3 columns were added to the start of the geochemical data spreadsheet: Jcode, Kcode, Lcode
2. The spreadsheet was saved as a text delimited txt file which was opened with IgPet
3. IgPet was used to plot Harker Diagrams, Tectonic Discrimination Diagrams and REE Spidergrams.

Rhyolite-MELTS

1. Sample PT18-013 was used as a starting composition in Rhyolite-MELTS as it was the most primitive basalt that conformed to the trends of the rest of the data
2. Starting composition
3. Temperature was set to 1400-850˚C and calculated at 5˚C intervals
4. Pressure was set to start and finish at 1000 bars
5. The oxidation state was set to Q Fa-Mt
6. Options → Fractionate Solids
7. Compute redox state to determine the approximate ratio of FeO to Fe_2O_3
8. Normalise to ensure that the composition totals 100%
9. After this model was run, the output was processed using an Excel macro provided from the MELTS website